

Formation and evolution of interstellar filaments

Hints from velocity dispersion measurements^{*,**}

D. Arzoumanian^{1,2}, Ph. André¹, N. Peretto¹, and V. Könyves^{1,2}

¹ Laboratoire AIM, CEA/DSM – CNRS – Université Paris Diderot, IRFU/Service d’Astrophysique, C.E.A. Saclay, Orme des Merisiers, 91191 Gif-sur-Yvette, France

e-mail: doris.arzoumanian@ias.u-psud.fr, pandre@cea.fr

² Present address: IAS, CNRS (UMR 8617), Université Paris-Sud, Bâtiment 121, 91400 Orsay, France

Received 29 November 2012 / Accepted 12 March 2013

ABSTRACT

We investigate the gas velocity dispersions of a sample of filaments recently detected as part of the *Herschel* Gould Belt Survey in the IC 5146, Aquila, and Polaris interstellar clouds. To measure these velocity dispersions, we use ¹³CO, C¹⁸O, and N₂H⁺ line observations obtained with the IRAM 30 m telescope. Correlating our velocity dispersion measurements with the filament column densities derived from *Herschel* data, we show that interstellar filaments can be divided into two regimes: thermally subcritical filaments, which have transonic velocity dispersions ($c_s \lesssim \sigma_{\text{tot}} < 2c_s$) independent of column density and are gravitationally unbound; and thermally supercritical filaments, which have higher velocity dispersions scaling roughly as the square root of column density ($\sigma_{\text{tot}} \propto \Sigma_0^{0.5}$) and which are self-gravitating. The higher velocity dispersions of supercritical filaments may not directly arise from supersonic interstellar turbulence but may be driven by gravitational contraction/accretion. Based on our observational results, we propose an evolutionary scenario whereby supercritical filaments undergo gravitational contraction and increase in mass per unit length through accretion of background material, while remaining in rough virial balance. We further suggest that this accretion process allows supercritical filaments to keep their approximately constant inner widths (~ 0.1 pc) while contracting.

Key words. stars: formation – ISM: clouds – ISM: structure – evolution – submillimeter: ISM

1. Introduction

Interstellar filaments have recently received special attention, thanks to the high quality and dynamic range of *Herschel*¹ observations (André et al. 2010; Men’shchikov et al. 2010; Molinari et al. 2010; Henning et al. 2010; Hill et al. 2011). The submillimeter dust continuum images of nearby molecular clouds (MCs) taken with the SPIRE (Griffin et al. 2010) and PACS (Poglitsch et al. 2010) cameras onboard *Herschel* provide key information on both dense cores on small scales (< 0.1 pc) and the filamentary structure of the parent clouds on large scales (> 1 pc), making it possible to investigate the physical connection between these two components of the cold interstellar medium (ISM) and to draw a more complete picture of star formation.

Already before *Herschel*, filamentary structures were known to be present in MCs (e.g., Schneider & Elmegreen 1979; Myers 2009) and appeared to be easily produced by any numerical simulation of MC evolution that includes hydrodynamic (HD) or magnetohydrodynamic (MHD) turbulence (e.g., Federrath et al. 2010; Hennebelle et al. 2008; Mac Low & Klessen 2004). Individual interstellar filaments have also been recently studied with molecular line observations (e.g., Pineda et al. 2011; Hacar & Tafalla 2011; Miettinen 2012; Bourke et al. 2012; Li & Goldsmith 2012). *Herschel* observations now demonstrate that

these filaments are truly ubiquitous in MCs and have a direct link to the formation process of prestellar cores (André et al. 2010; Palmeirim et al. 2013).

Filaments are detected with *Herschel* both in star-forming regions (Könyves et al. 2010; Bontemps et al. 2010), where they are associated with the presence of prestellar cores and protostars (André et al. 2010), and in non-star-forming regions, such as the Polaris translucent cloud (Men’shchikov et al. 2010; Miville-Deschênes et al. 2010; Ward-Thompson et al. 2010). These findings support the view that filament formation precedes any star-forming activity in MCs.

In a previous work (Arzoumanian et al. 2011), we characterized the physical properties of the filaments detected in three regions observed as part of the *Herschel* Gould Belt survey (HGBS, André et al. 2010) and found that all filaments share a roughly constant inner width of ~ 0.1 pc regardless of their central column density and environment. This result has been confirmed in other fields of the HGBS (Peretto et al. 2012; Palmeirim et al. 2013).

Observationally, only thermally supercritical filaments for which the mass per unit length exceeds the critical value ($M_{\text{line}} > M_{\text{line,crit}}$) show evidence of prestellar cores and the presence of star formation activity, whereas thermally subcritical filaments ($M_{\text{line}} < M_{\text{line,crit}}$) are generally devoid of *Herschel* prestellar cores and protostars (André et al. 2010). The critical mass per unit length, $M_{\text{line,crit}} = 2c_s^2/G$ (where c_s is the isothermal sound speed, and G is the gravitational constant), is the critical value required for a filament to be gravitationally unstable to radial contraction and fragmentation along its length (Inutsuka & Miyama 1997). Remarkably, this critical line mass $M_{\text{line,crit}}$ only depends on gas temperature (Ostriker 1964). It is approximately equal to $\sim 16 M_{\odot}/\text{pc}$ for gas filaments at $T = 10$ K, corresponding

* Based on observations carried out with the IRAM 30 m telescope. IRAM is supported by INSU/CNRS (France), MPG (Germany), and IGN (Spain).

** Appendix A available in electronic form at <http://www.aanda.org>

¹ *Herschel* is an ESA space observatory with science instruments provided by European-led Principal Investigator consortia and with important participation from NASA (Pilbratt et al. 2010).

to $c_s \sim 0.2 \text{ km s}^{-1}$. Assuming that interstellar filaments have Gaussian radial column density profiles, an estimate of the mass per unit length is given by $M_{\text{line}} \approx \Sigma_0 \times W_{\text{fil}}$ where W_{fil} is the typical filament width (see Appendix A of André et al. 2010 and Arzoumanian et al. 2011) and $\Sigma_0 = \mu m_{\text{H}} N_{\text{H}_2}^0$ is the central gas surface density of the filament.

For a typical filament width of $\sim 0.1 \text{ pc}$, the theoretical value of $M_{\text{line,crit}} \sim 16 M_{\odot}/\text{pc}$ (for $T \approx 10 \text{ K}$) corresponds to a central column density $N_{\text{H}_2}^0 \sim 8 \times 10^{21} \text{ cm}^{-2}$ (or visual extinction $A_V^0 \sim 8$). To first order, therefore, interstellar filaments may be divided into thermally supercritical and thermally subcritical filaments depending on whether their central column density $N_{\text{H}_2}^0$ is higher or lower than $\sim 8 \times 10^{21} \text{ cm}^{-2}$, respectively. Thermally supercritical filaments, with average column densities $\geq 8 \times 10^{21} \text{ cm}^{-2}$, are expected to be globally unstable to radial gravitational collapse and fragmentation into prestellar cores along their lengths. The prestellar cores formed in this way are themselves expected to collapse locally into protostars. Interestingly, the critical column density $\sim 8 \times 10^{21} \text{ cm}^{-2}$ of interstellar filaments is very close to the star formation threshold at a background extinction $A_V \sim 6\text{--}9$ above which the bulk of prestellar cores and young stellar objects are observed in nearby clouds (e.g., Johnstone et al. 2004; Goldsmith et al. 2008; Heiderman et al. 2010; Lada et al. 2010; André et al. 2010, 2011).

The results summarized above on the properties of interstellar filaments were made possible thanks to the sensitivity and resolution of the HGBS observations, which allowed us to detect structures down to $A_V \sim 0.1$ and to resolve individual filaments in nearby regions ($d < 0.5 \text{ kpc}$), down to a typical Jeans length of $\sim 0.02 \text{ pc}$. While the *Herschel* images already are a powerful tool to assess the importance of different physical processes involved in the formation and evolution of interstellar filaments, they do not provide any information on the underlying kinematics of the gas.

In the present work, we complement our first results obtained from *Herschel* imaging data with molecular line observations to gain insight into the velocity dispersion of the interstellar filaments and reinforce our understanding of filament formation and evolution. We present ^{13}CO , C^{18}O , and N_2H^+ line observations, taken with the IRAM 30 m-telescope, toward a sample of filaments detected with *Herschel* in the IC 5146, Aquila Rift, and Polaris flare regions. In Sect. 2 we present the observations and the data reduction. Sections 3 and 4 summarize the data analysis, Sect. 5 presents the results and Sect. 6 discusses their implications in the proposed scenario for interstellar filament formation and evolution.

2. IRAM observations and data reduction

Molecular line observations of a sample of filaments in IC 5146, Aquila, and Polaris were carried on at the IRAM-30 m telescope at Pico Veleta, Spain, during two observing runs in March and August 2011.

In March 2011, we observed the $\text{C}^{18}\text{O}(2\text{--}1)$ and $^{13}\text{CO}(2\text{--}1)$ spectral lines with the HETerodyne Receiver Array (HERA, Schuster et al. 2004) and the $\text{N}_2\text{H}^+(1\text{--}0)$ line with the Eight MIXer Receiver (EMIR, a multiband mm-wave receiver, Carter et al. 2012) toward the filaments of IC 5146. In addition to single-position spectra taken in the on-off observing mode, we mapped filament 14 in IC 5146 (yellow rectangle in Fig. 1) in the $\text{C}^{18}\text{O}(2\text{--}1)$ and $^{13}\text{CO}(2\text{--}1)$ transitions using the on-the-fly mapping mode with HERA. The Aquila rift and the Polaris clouds

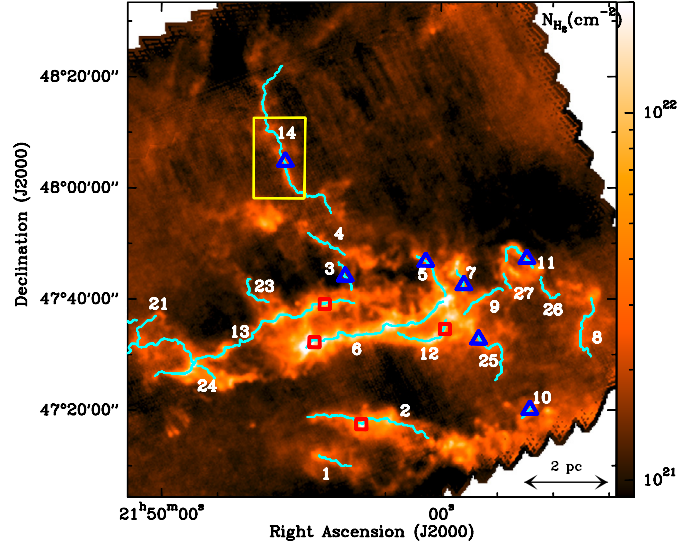


Fig. 1. *Herschel* column density map of the northern and southern streamers of IC 5146 with the network of filaments highlighted in blue (adapted from Fig. 3b of Arzoumanian et al. 2011). The positions of the observed spectra are plotted as red squares and blue triangles for N_2H^+ and C^{18}O , respectively (the corresponding spectra of the positions observed for filament 2 and filament 14 are shown in Fig. 2). The yellow rectangle shows the subcritical filament 14 which was mapped in $\text{C}^{18}\text{O}(2\text{--}1)$ and $^{13}\text{CO}(2\text{--}1)$; cf. Fig. 3.

were observed in August 2011 in the $\text{C}^{18}\text{O}(1\text{--}0)$ and $\text{N}_2\text{H}^+(1\text{--}0)$ transitions with EMIR.

The spatial resolutions of the observations correspond to the $12''$, $23''$ and $28''$ FWHM beamwidths of the 30 m antenna at 219.6 GHz [$\text{C}^{18}\text{O}(2\text{--}1)$], 109.8 GHz [$\text{C}^{18}\text{O}(1\text{--}0)$], and 93.2 GHz [$\text{N}_2\text{H}^+(1\text{--}0)$], respectively. We used the VESPA autocorrelator as backend with a spectral resolution of 20 KHz. This spectral resolution translates to velocity resolutions of 0.027, 0.055, and 0.064 km s^{-1} at the frequencies of the $\text{C}^{18}\text{O}(2\text{--}1)$, $\text{C}^{18}\text{O}(1\text{--}0)$, and $\text{N}_2\text{H}^+(1\text{--}0)$ transitions, respectively.

We used the frequency-switching mode for the CO observations and the position-switching mode for the N_2H^+ observations, using a reference position offset by $\sim 10'\text{--}15'$ from each target position. The off position was selected from the *Herschel* images and the lack of N_2H^+ emission was checked using observations in the frequency-switching mode. During the observations, calibration was achieved by measuring the emission from the sky, an ambient load and a cold load every $\sim 15 \text{ min}$. The telescope pointing was checked and adjusted every $\sim 2 \text{ h}$ and the pointing accuracy was found to be better than $3''$. The typical rms of each single position (on-off mode) spectrum is $\sim 0.05 \text{ K}$ (in T_{A}^* scale). All of the data were reduced with the GILDAS/CLASS software package (the Grenoble Image and Line Data Analysis System, a software provided and actively developed by IRAM²).

2.1. Filament sample

A total number of 100 positions toward 70 filaments or segments of filaments³ were observed in the three regions (IC 5146, Aquila, Polaris). Most of the densest filaments, with $N_{\text{H}_2} \gtrsim 1 \times 10^{22} \text{ cm}^{-2}$, were detected in $\text{N}_2\text{H}^+(1\text{--}0)$, which is a low

² <http://www.iram.fr/IRAMFR/GILDAS>

³ Due to the presence of apparent intersections of filamentary structures in the plane of the sky, there is sometimes some ambiguity in the definition of an “individual filament”.

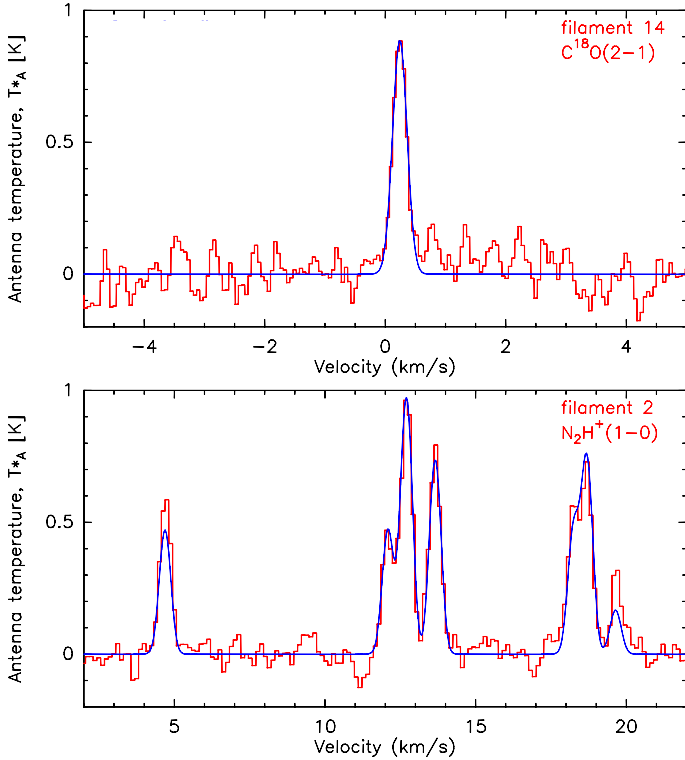


Fig. 2. Spectra observed in the $C^{18}O(2-1)$ and the $N_2H^+(1-0)$ transitions, toward filament 14 (*top*) and 2 (*bottom*), respectively. The best Gaussian fits to the spectra are overlaid in blue. The fitted parameters are given in Table 1.

optical depth tracer of dense gas, as well as in $C^{18}O$ and ^{13}CO . The lower column density filaments were only detected in $C^{18}O$ and ^{13}CO , while the faintest filaments were not detected⁴.

The final sample discussed in the remainder of this paper corresponds to the 46 filaments detected in either N_2H^+ or $C^{18}O$. This sample consists of 44 individual filaments detected with the IRAM 30 m telescope in IC 5146 (11 filaments), Aquila rift (26 filaments), and Polaris flare (7 filaments), plus 2 filaments corresponding to the NGC 2264C elongated clump (Peretto et al. 2006) and the DR21 ridge (Schneider et al. 2010; Hennemann et al. 2012).

The positions of the filaments observed in IC 5146 are shown in Fig. 1, overlaid on the *Herschel* column density map. The filaments observed in Aquila and Polaris are shown in Figs. A.5, A.8 and A.10, respectively. A N_2H^+ (1-0) spectrum and a $C^{18}O(2-1)$ spectrum toward two filaments observed in IC 5146 are shown in Fig. 2. The positions and derived parameters of all the filaments used for the analysis presented in this paper are summarized in Table 1 and the corresponding spectra are shown in online Appendix A.

3. Line-of-sight velocity dispersions

In order to combine the velocity information obtained with various line tracers, we estimated the total velocity dispersion of the mean free particle in molecular clouds.

⁴ A few filaments observed in IC 5146 (5 filaments) and Polaris (1 filament) were only detected in ^{13}CO . The velocity dispersions ($\sim 0.3 \text{ km s}^{-1}$ on average) of these filaments were not included in the filament sample due to larger uncertainties in the optical depth of this transition.

We estimated the non-thermal velocity dispersion of the gas by subtracting the thermal velocity dispersion from the linewidth measured for each species, assuming that the two contributions are independent of each other and could be added in quadrature (Myers 1983). The thermal velocity dispersion of each species is given by

$$\sigma_T(\mu_{\text{obs}}) = \sqrt{\frac{k_B T}{\mu_{\text{obs}} m_H}}, \quad (1)$$

where k_B is the Boltzmann constant, μ_{obs} is the atomic weight of the observed molecule, i.e. $\mu_{\text{obs}} = 29$ for N_2H^+ and $\mu_{\text{obs}} = 30$ for $C^{18}O$. We adopted a gas temperature of 10 K which is the typical temperature of starless molecular clouds and is close to the dust temperature measured with *Herschel* for the present sample of filaments. The non-thermal velocity dispersion is then equal to

$$\sigma_{\text{NT}} = \sqrt{\sigma_{\text{obs}}^2 - \sigma_T^2(\mu_{\text{obs}})}, \quad (2)$$

where $\sigma_{\text{obs}} = \Delta V / \sqrt{8 \ln 2}$ and ΔV is the measured FWHM linewidth of the observed spectra. The linewidths were estimated by single Gaussian fits to the $C^{18}O$ spectra (cf. Appendix A for more details) and by multiple Gaussian fits to the seven components of the hyperfine multiplet of the N_2H^+ transition, using the Gaussian HyperFine Structure (HFS) fitting routine of the CLASS software package. This routine derives the line optical depth by assuming the same excitation temperature for all hyperfine components, and therefore yields an estimate of the intrinsic linewidth.

The total velocity dispersion of the mean free particle of molecular weight $\mu = 2.33$ is finally given by:

$$\sigma_{\text{tot}}(\mu) = \sqrt{\sigma_{\text{NT}}^2 + \sigma_T^2(\mu)}, \quad (3)$$

where $\sigma_T(\mu) = \sqrt{\frac{k_B T}{\mu m_H}} \sim 0.2 \text{ km s}^{-1}$ for $T = 10 \text{ K}$. The typical gas temperature in the center of the dense filaments of our sample is approximately $T_{\text{gas}} \sim 10 \text{ K}$ since the dust temperature derived from *Herschel* data is $T_{\text{dust}} \sim 10 \text{ K}$ and T_{gas} is expected to be well coupled to T_{dust} at densities $\gtrsim 3 \times 10^4 \text{ cm}^{-3}$ (see Galli et al. 2002). As to the lower-density filaments in our sample, CO observations directly show that their gas temperature is also close to 10 K (e.g., Goldsmith et al. 2008; Heyer et al. 2009).

4. Velocity dispersion along filament 14 in IC 5146

The velocity dispersions of the filaments in our sample have been estimated from single-position observations toward each filament. To assess the reliability of inferring the velocity dispersion of a filament from a single position spectrum, we investigated the variations of the velocity dispersion along the crest of filament 14 in IC 5146 which we mapped in both $^{13}CO(2-1)$ and $C^{18}O(2-1)$ – see Fig. 3.

From the $^{13}CO(2-1)/C^{18}O(2-1)$ ratio map, we first estimated the optical depth to check whether or not the $C^{18}O(2-1)$ emission is optically thin.

Assuming uniform excitation temperature along the line of sight, $^{13}CO(2-1)$ and $C^{18}O(2-1)$ line emissions can be expressed as a function of optical depth as follows:

$$T_A^{*,i}(v) = T_{\text{ex}}^i [1 - \exp(-\tau^i(v))], \quad (4)$$

where i corresponds to either $C^{18}O(2-1)$ or $^{13}CO(2-1)$, $T_A^{*,i}(v)$ is the detected antenna temperature for each velocity channel v ,

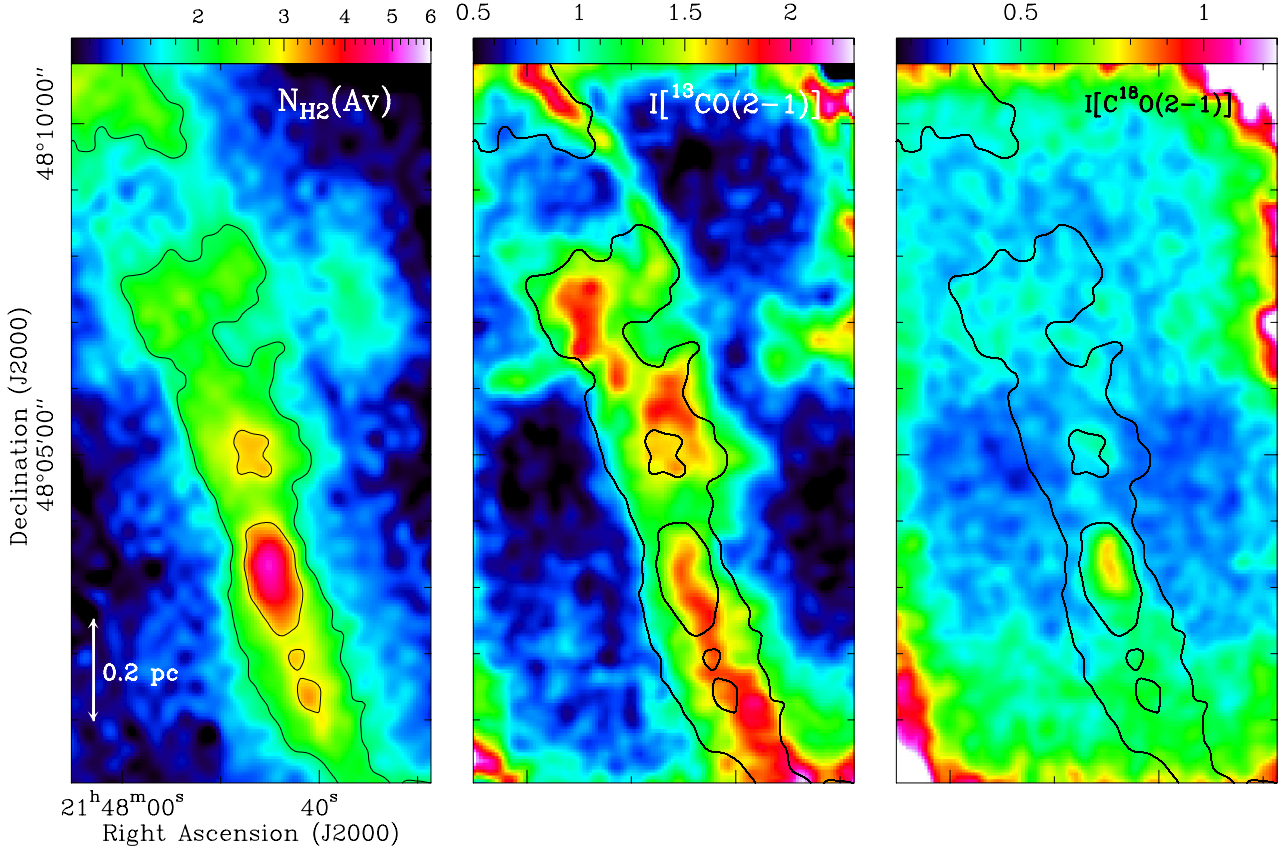


Fig. 3. *Left:* *Herschel* column density map of filament 14 in IC 5146 corresponding to the yellow rectangle in Fig. 1, in units of visual extinction (A_V) where $N_{\text{H}_2} \sim A_V \times 10^{21} \text{ cm}^{-2}$. The resolution of the map is $36.9''$. The black contours correspond to column densities of 1 and $2 \times 10^{21} \text{ cm}^{-2}$. These contours are reproduced in the *middle and right panels*. *Middle:* $^{13}\text{CO}(2-1)$ integrated intensity map (in units of K km s^{-1}) over the LSR velocity range -2.5 to 1 km s^{-1} . The map has been smoothed to a resolution of $18.5''$, which corresponds to half the resolution of the *Herschel* column density map. The $^{13}\text{CO}(2-1)$ integrated emission of the filament is concentrated within the 10^{21} cm^{-2} column density contour, which traces the elongated structure of the filament. *Right:* same as the *middle panel* for the $\text{C}^{18}\text{O}(2-1)$ transition.

T_{ex}^i is the excitation temperature which we assume to be the same for the two isotopomers and τ_{21}^i is the optical depth of the (2–1) transition of C^{18}O or ^{13}CO .

The optical depth values at the systemic velocity (v_{sys}) of the cloud for each transition were estimated from the ratio of the $^{13}\text{CO}(2-1)$ and $\text{C}^{18}\text{O}(2-1)$ line intensities:

$$\frac{T_{\text{A}}^{*,13}(v_{\text{sys}})}{T_{\text{A}}^{*,18}(v_{\text{sys}})} = \frac{T_{\text{ex}}^{13}[1 - \exp(-\tau_{21}^{13}(v_{\text{sys}}))]}{T_{\text{ex}}^{18}[1 - \exp(-\tau_{21}^{18}(v_{\text{sys}}))]}, \quad (5)$$

where $T_{\text{ex}}^{13} = T_{\text{ex}}^{18}$ and $\tau_{21}^{13} = X\tau_{21}^{18}$, with $X = [^{13}\text{CO}]/[\text{C}^{18}\text{O}] = 5.5$ (the assumed mean value of the abundance ratio in the local ISM, e.g. [Wilson & Rood 1994](#)).

Maps of the mean optical depth of filament 14 were constructed from the observed integrated intensity ratio map of the $^{13}\text{CO}(2-1)$ and $\text{C}^{18}\text{O}(2-1)$ transitions, over the velocity range -2.5 to $+1 \text{ km s}^{-1}$,

$$R_{13/18} = \int_{-2.5}^1 T_{\text{A}}^{*,13}(v)dv / \int_{-2.5}^1 T_{\text{A}}^{*,18}(v)dv.$$

We estimated the mean values of τ_{21}^{18} and τ_{21}^{13} (corresponding to the optical depth values integrated over the velocity range -2.5 to $+1 \text{ km s}^{-1}$) from the $R_{13/18}$ ratio map by solving a velocity-integrated form of Eq. (5) on a pixel by pixel basis. Figure 4 shows the mean optical depth maps of the $^{13}\text{CO}(2-1)$ and $\text{C}^{18}\text{O}(2-1)$ transitions for filament 14 (*middle and right panels*, respectively) along with the $R_{13/18}$ ratio map (*left panel*).

While the bulk of the C^{18}O emission is optically thin ($\tau_{21}^{18} < 0.6$) along the main axis of the filament, the ^{13}CO emission is significantly optically thick ($\tau_{21}^{13} > 2$) in the southern half part of the filament and only marginally optically thin ($\tau_{21}^{13} \sim 0.5-2$) in the northern part of the filament.

Figure 5 shows the positions along filament 14 where spectra were extracted from the maps (left-hand side of the figure) and the velocity dispersions measured along the filament (right). The velocity dispersions derived from the $^{13}\text{CO}(2-1)$ spectra were corrected for the broadening effect due to the finite optical depth of the $^{13}\text{CO}(2-1)$ transition. To do so, we measured the variations of the FWHM linewidth, ΔV_{obs} , of a simple Gaussian line model, $T_{\tau_0}^{\text{model}}(v)$, as a function of optical depth. The model line spectrum had the form $T_{\tau_0}^{\text{model}}(v) = T_{\text{ex}}[1 - \exp(-\tau(v))]$, where T_{ex} is a uniform excitation temperature, $\tau(v) = \tau_0 \exp\left[-\frac{4 \ln 2 (v-v_0)^2}{\Delta V_{\text{int}}^2}\right]$ corresponds to an intrinsically Gaussian distribution of optical depths with velocity, v , and ΔV_{int} is the intrinsic FWHM linewidth of the model. By fitting Gaussian profiles to synthetic spectra, we estimated the FWHM width ΔV_{obs} of the model as a function of τ_0 , and derived correction factors $\Delta V_{\text{int}}/\Delta V_{\text{obs}} \approx 0.77-0.92$, for $^{13}\text{CO}(2-1)$ optical depths ranging between 0.5 and 2.5. The most extreme correction would be a factor of 0.74 for a $^{13}\text{CO}(2-1)$ optical depth of 3, if the $[^{13}\text{CO}]/[\text{C}^{18}\text{O}]$ abundance ratio has a value of 7 (e.g., [Wu et al. 2012](#)), i.e., higher than the standard value in the local ISM.

Inspection of the linewidths measured along filament 14 shows that the variations of the internal velocity dispersion are

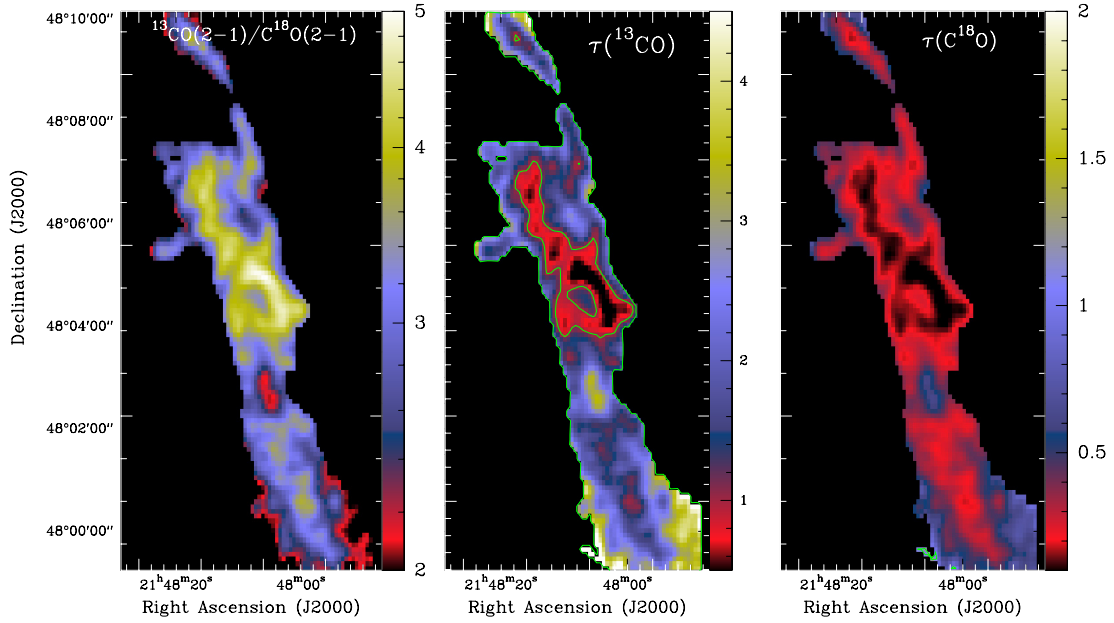


Fig. 4. *Left:* integrated intensity ratio map $\int_{-2.5}^1 T_A^{*,13}(\nu)d\nu / \int_{-2.5}^1 T_A^{*,18}(\nu)d\nu$ for filament 14 in IC 5146. Only those pixels where the column density derived from *Herschel* is higher than 10^{21} $\text{H}_2 \text{cm}^{-2}$ have been considered (black contour in Fig. 3). *Middle:* map of the mean optical depth of the $^{13}\text{CO}(2-1)$ transition. The contours in green correspond to a value of 1. *Right:* map of the mean optical depth of the $\text{C}^{18}\text{O}(2-1)$ transition. The mean optical depth of the C^{18}O transition is $\tau(\text{C}^{18}\text{O}) < 1$ over the entire filament.

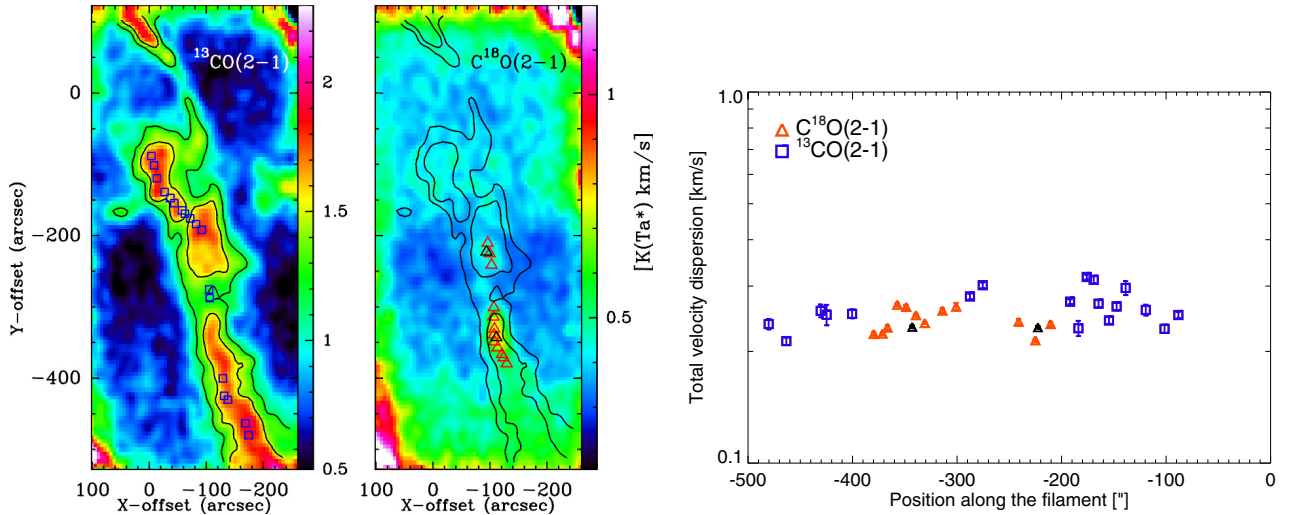


Fig. 5. *Left:* integrated $^{13}\text{CO}(2-1)$ and $\text{C}^{18}\text{O}(2-1)$ intensity maps of filament 14 in IC 5146 (cf. Fig. 3). Two $^{13}\text{CO}(2-1)$ contours are overlaid: 1.2 and 1.5 K km s^{-1} . The blue squares and red triangles correspond to the positions along the filament where the line-of-sight velocity dispersion has been measured from the $^{13}\text{CO}(2-1)$ and $\text{C}^{18}\text{O}(2-1)$ maps respectively. The two black triangles on the $\text{C}^{18}\text{O}(2-1)$ map correspond to the positions of the central pixel of the array receiver of HERA observed in a single pointing. The labels indicate the offsets in arcsec relative to the center of the map at $\text{Ra}(\text{J2000}) = 21:47:56$ and $\text{Dec}(\text{J2000}) = 48:08:55$. The black triangle at position $(-94'', -223'')$ is the point which represents filament 14 in the column density vs. velocity dispersion diagram (black triangle in Fig. 6). *Right:* total velocity dispersions, σ_{tot} (see Eq. (3)), measured along the same filament. The x -axis goes from the south to the north of the filament. The red triangle and blue squares correspond to measurements made on the $\text{C}^{18}\text{O}(2-1)$ and $^{13}\text{CO}(2-1)$ maps, respectively. Individual spectra were constructed by spatially averaging the signal located within $10''$ of the central position to increase the signal to noise ratio of the data. The linewidths of the $^{13}\text{CO}(2-1)$ spectra were corrected for the broadening due to optical depth effects (see explanations in Sect. 4). The median value of σ_{tot} is 0.25 km s^{-1} with a narrow dispersion of 0.03 km s^{-1} .

small along the crest of the filament (cf. right panel of Fig. 5), with an average velocity dispersion $(0.25 \pm 0.03) \text{ km s}^{-1}$. This is consistent with previous observations of a few low-density filaments showing that these structures have velocity dispersions close to the thermal velocity dispersion $\sim 0.2 \text{ km s}^{-1}$ for $T = 10 \text{ K}$ (cf. Hily-Blant 2004; Hily-Blant & Falgarone 2009) and which do not vary much along their length (Hacar & Tafalla 2011; Pineda et al. 2011). Recently, Li & Goldsmith (2012) studied the Taurus B213 filament and found that it is characterized by a coherent velocity dispersion of about $\sim 0.3 \text{ km s}^{-1}$.

These results suggest that the velocity dispersion observed at a single position toward a filament provides a reasonably good estimate of the velocity dispersion of the entire filament⁵. Nevertheless mapping observations of a broader sample

⁵ An interstellar filament is an elongated structure characterized by small column density variations along its crest (less than a factor of 3; see Fig. 3-left). Therefore, the velocity dispersion variations induced by the trend $\sigma_{\text{tot}} \propto \Sigma_0^{0.5}$ found in Sect. 5 below for supercritical filaments remain small ($\ll 2$) along a given filament.

Table 1. Summary of derived parameters of the observed spectra toward the filaments of our sample.

Field/tracer	Filament	Ra (J2000)	Dec (J2000)	N_{H_2} [10^{21} cm^{-2}]	M_{line} M_{\odot}/pc	V_{LSR} [km s^{-1}]	T_{peak} [$\text{K}(T_{\text{A}}^*)$]	rms	σ_{obs} [km s^{-1}]	σ_{tot} [km s^{-1}]	$\sigma_{\text{tot}}^{\text{err}}$
(1)	(2)	(3)	(4)	(5)	(6)	(7)	(8)	(9)	(10)	(11)	(12)
Aquila $\text{N}_2\text{H}^+(1-0)$	1	18:29:39.5	-01:50:14	213.4	252	7.70	1.43	0.67	0.60	0.64	0.01
	2	18:32:38.5	-02:50:24	40.9	176	7.85	0.67	0.22	0.30	0.36	0.01
	3	18:33:15.2	-02:48:14	13.0	35	6.42	0.65	0.13	0.11	0.23	0.01
	4	18:33:06.7	-02:47:50	11.6	32	7.04	0.26	0.08	0.11	0.23	0.01
	5	18:33:22.5	-02:42:30	12.8	20	6.84	0.16	0.05	0.15	0.25	0.01
	6	18:29:36.6	-01:51:55	13.2	39	7.63	0.12	0.05	0.11	0.23	0.01
	7	18:29:50.4	-01:54:47	37.9	123	7.67	1.18	0.25	0.18	0.27	0.01
	8	18:30:27.6	-01:55:32	35.2	139	7.42	0.41	0.13	0.20	0.28	0.01
	9	18:30:19.1	-01:53:09	33.9	90	7.72	0.18	0.11	0.41	0.45	0.01
	10	18:29:08.9	-01:42:40	29.9	121	7.05	0.76	0.18	0.21	0.29	0.01
	11	18:29:19.9	-01:52:25	25.1	68	7.27	0.32	0.09	0.23	0.31	0.01
	12	18:30:03.9	-02:04:29	20.3	73	7.12	0.68	0.19	0.19	0.27	0.06
	13	18:29:55.8	-02:00:18	74.5	182	7.09	1.39	0.60	0.42	0.47	0.01
	14	18:29:58.1	-01:57:38	55.8	265	7.41	0.45	0.21	0.44	0.48	0.01
	15	18:28:50.1	-01:34:52	114.1	288	7.90	0.79	0.23	0.36	0.41	0.01
	16	18:30:03.5	-02:02:26	10.9	35	7.36	0.37	0.07	0.10	0.22	0.01
	17	18:29:55.4	-01:37:02	12.0	40	8.29	0.53	0.12	0.14	0.24	0.01
	18	18:29:34.6	-01:55:15	9.2	38	7.34	0.10	0.04	0.15	0.25	0.01
IC 5146 $\text{N}_2\text{H}^+(1-0)$	2	21:46:28.1	47:17:34	25.3	80	4.69	0.61	0.17	0.19	0.27	0.01
	6	21:47:17.2	47:33:01	17.0	109	3.69	0.32	0.11	0.25	0.32	0.01
	12	21:44:58.4	47:34:15	14.7	41	4.11	0.40	0.13	0.19	0.28	0.01
	13	21:47:07.9	47:39:30	17.1	50	4.35	0.25	0.10	0.22	0.30	0.01
Polaris $\text{N}_2\text{H}^+(1-0)$	1	02:00:29.0	87:41:54	8.0	16	-4.62	0.18	0.01	0.13	0.24	0.01
Aquila $\text{C}^{18}\text{O}(1-0)$	19	18:29:53.5	-03:43:39	7.9	10	4.88	1.22	0.06	0.23	0.31	0.01
	20	18:28:58.2	-01:22:51	7.8	28	7.17	1.10	0.04	0.30	0.36	0.01
	21	18:31:06.4	-01:18:58	9.9	20	7.77	1.10	0.05	0.26	0.33	0.01
	22	18:33:15.8	-02:47:15	7.2	51	6.47	1.26	0.03	0.13	0.24	0.01
	23	18:22:51.1	-03:26:38	6.3	12	5.78	0.36	0.03	0.28	0.34	0.01
	24	18:23:31.3	-03:03:43	7.2	15	6.87	0.89	0.03	0.27	0.34	0.01
	25	18:29:45.6	-02:32:21	7.3	22	6.52	0.94	0.03	0.15	0.25	0.01
	26	18:32:53.1	-01:29:42	7.0	21	7.28	0.28	0.03	0.16	0.26	0.01
IC 5146 $\text{C}^{18}\text{O}(2-1)$	3	21:46:42.1	47:44:26	2.8	3	1.89	0.80	0.08	0.17	0.26	0.01
	5	21:45:15.3	47:46:52	3.0	11	1.42	0.63	0.09	0.24	0.31	0.02
	7	21:44:37.1	47:42:39	5.2	11	3.71	0.76	0.09	0.29	0.35	0.02
	10	21:43:29.1	47:19:29	4.3	16	4.21	0.79	0.06	0.13	0.24	0.01
	11	21:43:30.9	47:47:12	3.1	9	3.29	0.42	0.08	0.11	0.23	0.01
	14	21:47:48.1	48:04:53	3.9	15	0.24	0.89	0.07	0.12	0.23	0.01
25	21:44:18.8	47:32:25	5.7	17	2.32	0.47	0.09	0.27	0.34	0.03	
Polaris $\text{C}^{18}\text{O}(1-0)$	2	01:58:59.7	87:39:33	9.6	16	-4.29	2.65	0.04	0.22	0.29	0.01
	3	01:40:31.4	87:46:19	2.4	15	-4.14	0.28	0.04	0.22	0.30	0.02
	4	01:31:21.7	87:45:56	2.7	25	-4.48	0.27	0.03	0.19	0.27	0.02
	5	02:00:49.1	87:35:18	3.4	15	-4.08	0.62	0.04	0.17	0.30	0.01
	6	01:50:48.0	87:43:47	1.5	3	-3.46	0.19	0.04	0.19	0.28	0.02
	7	03:36:47.4	88:08:13	2.3	16	-3.39	0.12	0.05	0.08	0.26	0.01

Notes. Columns 3 and 4: Equatorial coordinates providing the positions of the observed spectra. Columns 5 and 6: Projected column density and mass per unit length for each filament measured from *Herschel* column density maps. The listed values have not been corrected by the 60% systematic overestimation of true column densities and masses per unit length. All the filaments detected in N_2H^+ are supercritical while most of the filaments observed in $\text{C}^{18}\text{O}(1-0)$ and $(2-1)$ and not detected in N_2H^+ are subcritical. Columns 7, 8 and 10: parameters of single and multiple Gaussian fits to the C^{18}O and N_2H^+ observed spectra, respectively. For the N_2H^+ spectra T_{peak} (Col. 8) corresponds to the peak temperature of the isolated component of the N_2H^+ multiplet. Column 9 gives the corresponding rms. The reference positions used for the position-switched N_2H^+ observations were selected from the *Herschel* images and correspond to 21:47:22.6 47:45:59 for IC 5146, 01:56:30.26 87:43:28 for Polaris, 18:28:23.9 -02:00:22 for Aquila, except for filaments 3, 4 and 5 for which a reference position at 18:33:27.75 -02:51:22 was used. Columns 10 and 11: σ_{obs} and σ_{tot} are derived as explained in Sect. 3.

of filaments in several regions would be valuable to confirm the robustness of this assumption.

5. Two regimes for interstellar filaments

In this section, we investigate the variation of internal velocity dispersion with column density for our sample of filaments.

Figure 6 shows the total velocity dispersion as a function of central column density for the 46 filaments. Values for the column density and velocity dispersion of the NGC 2264C elongated clump (red square in the following plots) are taken from Peretto et al. (2006). Peretto et al. estimated the column density from 1.2 mm dust continuum mapping observations and the velocity dispersion of NGC 2264C from $\text{N}_2\text{H}^+(1-0)$

observations, both obtained with the IRAM 30 m telescope. The velocity dispersion was averaged over the entire NCG 2264C clump and reflects the velocity dispersion of the filamentary clump as opposed to the embedded protostellar cores. The velocity dispersion of the DR21 filament (green square in the following plots) is taken from Schneider et al. (2010) who derived it from $N_2H^+(1-0)$ observations, while the column density of DR21 comes from *Herschel* observations (Hennemann et al. 2012) obtained as part of the HOBYS key project (Motte et al. 2010). The black triangle corresponds to filament 14 in IC 5146 and the associated error bar comes from the dispersion of the total velocity dispersion along this filament as extracted from the map shown in Fig. 5. The vertical error bars of the other points correspond to the errors in estimating the linewidth from Gaussian fits to the observed spectra, which are on the order of $\sim 0.01 \text{ km s}^{-1}$. The error on the measured velocity dispersion is $\sim 0.03 \text{ km s}^{-1}$ for the filaments observed in Aquila and IC 5146 and 0.1 km s^{-1} for DR21 and NGC 2264C (representing the variation of σ_{tot} along the filament crests). The errors on the filament central column densities come from the uncertainties in deriving column densities⁶ from *Herschel* dust continuum maps and are typically a factor of ~ 2 mainly due to uncertain assumptions concerning the adopted dust opacity law (see Könyves et al. 2010; Arzoumanian et al. 2011). A recent study comparing *Herschel* and near-IR extinction data in Orion A reported a weak trend between dust opacity and column density, at least in the regime $1 \lesssim A_V \lesssim 10$, which has been interpreted as evidence of dust grain evolution with environment (Roy et al. 2013). But the uncertainty induced by this effect remains small for most of the filaments in our sample.

An additional systematic effect on the column density comes from the random inclination angles of the filaments to the plane of the sky, which implies an overestimation of the intrinsic column densities (and masses per unit length) by $\sim 60\%$ on average for a large sample of filaments (for more details see Appendix A of Arzoumanian et al. 2011). This systematic correction factor is shown as a horizontal arrow pointing to the left in Fig. 6.

The results of our velocity dispersion measurements confirm that the filaments of our sample can be divided into two physically distinct groups based on their central column density. Filaments with column densities $\leq 8 \times 10^{21} \text{ cm}^{-2}$ seem to have roughly constant velocity dispersions close to or slightly larger than the sound speed ($c_s \lesssim \sigma_{\text{tot}} < 2c_s$), while denser filaments with column densities $\geq 8 \times 10^{21} \text{ cm}^{-2}$ have velocity dispersions which increase as a function of column density (cf. Fig. 6). The upper x -axis of Fig. 6 shows an approximate mass-per-unit-length scale derived from the bottom x -axis scale by multiplying the central column density of each filament by a characteristic filament width $W_{\text{fil}} \sim 0.1 \text{ pc}$ (i.e., $M_{\text{line}} = \Sigma_0 \times W_{\text{fil}}$ – see Sect. 1). It can be seen from Fig. 6 that the critical mass per unit length $M_{\text{line,crit}} \sim 16 M_{\odot}/\text{pc}$ for $T \approx 10 \text{ K}$ introduced in Sect. 1 corresponds to a column density boundary which divides the filaments into two regimes where thermally subcritical filaments ($M_{\text{line}} < M_{\text{line,crit}}$) have roughly constant velocity dispersions with a mean value of $0.26 \pm 0.05 \text{ km s}^{-1}$, while thermally supercritical filaments ($M_{\text{line}} > M_{\text{line,crit}}$) have velocity dispersions which increase as a function of projected column density as a

⁶ The column densities were derived consistently for all filaments observed with *Herschel* in Polaris, IC 5146, Aquila, and DR21. The same dust opacity law was used to derive the column density of NGC 2264C from MAMBO 1.2 mm continuum observations. The column density estimates for NGC 2264C and DR21 are more uncertain due to the presence of prominent cores along the filament crests (cf. Peretto et al. 2006; Motte et al. 2007).

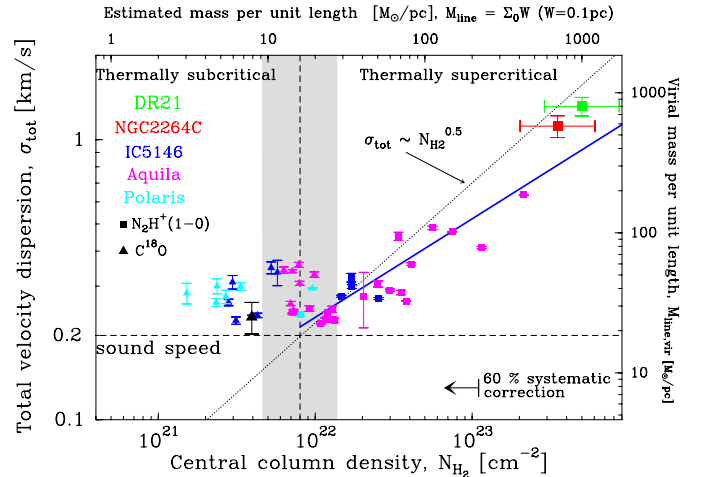


Fig. 6. Total velocity dispersion versus observed central column density (uncorrected for inclination effects): blue for IC 5146, magenta for Aquila, cyan for Polaris, red for NGC 2264C, and green for DR21 filaments. The squares and triangles correspond to velocity dispersions measured from N_2H^+ spectra and $C^{18}O$ spectra, respectively. See text for details on the error bars and for uncertainties in the column densities. The horizontal dashed line shows the value of the sound speed $\sim 0.2 \text{ km s}^{-1}$ for $T = 10 \text{ K}$. The vertical dashed line marks the boundary between thermally subcritical and thermally supercritical filaments where the estimated mass per unit length M_{line} is approximately equal to the critical value $M_{\text{line,crit}} \sim 16 M_{\odot}/\text{pc}$ for $T = 10 \text{ K}$, equivalent to a column density of $8 \times 10^{21} \text{ cm}^{-2}$. The grey band shows a dispersion of a factor of 3 around this nominal value. The dotted line running from the bottom left to the top right corresponds to $\sigma_{\text{tot}} \propto N_{H_2}^{0.5}$ normalized to 0.2 km s^{-1} at the subcritical/supercritical boundary. The blue solid line shows the best power-law fit $\sigma_{\text{tot}} \propto N_{H_2}^{0.35 \pm 0.14}$ to the supercritical filaments.

power law $\sigma_{\text{tot}} \propto N_{H_2,\text{obs}}^{0.35 \pm 0.14}$. The latter relation becomes $\sigma_{\text{tot}} \propto N_{H_2,\text{corr}}^{0.41 \pm 0.15}$ if “intrinsic” column density values are used (after correcting the observed values for a $\sim 60\%$ overestimation on average due to inclination effects). The division of the filament sample into two regimes does not correspond to a sharp boundary but to a narrow border zone represented by the grey band in Fig. 6 which results from 1) a spread of a factor of $\lesssim 2$ in the effective width of the filaments around the nominal value of 0.1 pc used to convert the critical mass per unit length to a critical column density; 2) uncertainties in the intrinsic column densities of the filaments due to a random distribution of viewing angles; and 3) a small dispersion in the effective gas temperature of the filaments, implying a small spread in the theoretical value of the effective critical mass per unit length (see below).

To derive more accurate filament masses per unit length, we constructed radial column density profiles from the *Herschel* column density maps, taking a perpendicular cut to each filament at the position observed with the 30 m telescope. The observed mass per unit length, $M_{\text{line}}^{\text{obs}}$, of each filament was then derived by integrating the measured column density profile over radius. The mass per unit length of DR21 corresponds to the average value along the crest of the filament derived by Hennemann et al. (2012), while the value for NGC 2264C was obtained from its estimated mass ($1650 M_{\odot}$) and length (0.8 pc). These $M_{\text{line}}^{\text{obs}}$ estimates of the mass per unit length are used in the following discussion instead of the simpler estimates shown at the top of Fig. 6.

Figure 7a shows the total velocity dispersion of each filament (same y -axis as in Fig. 6) as a function of the estimated

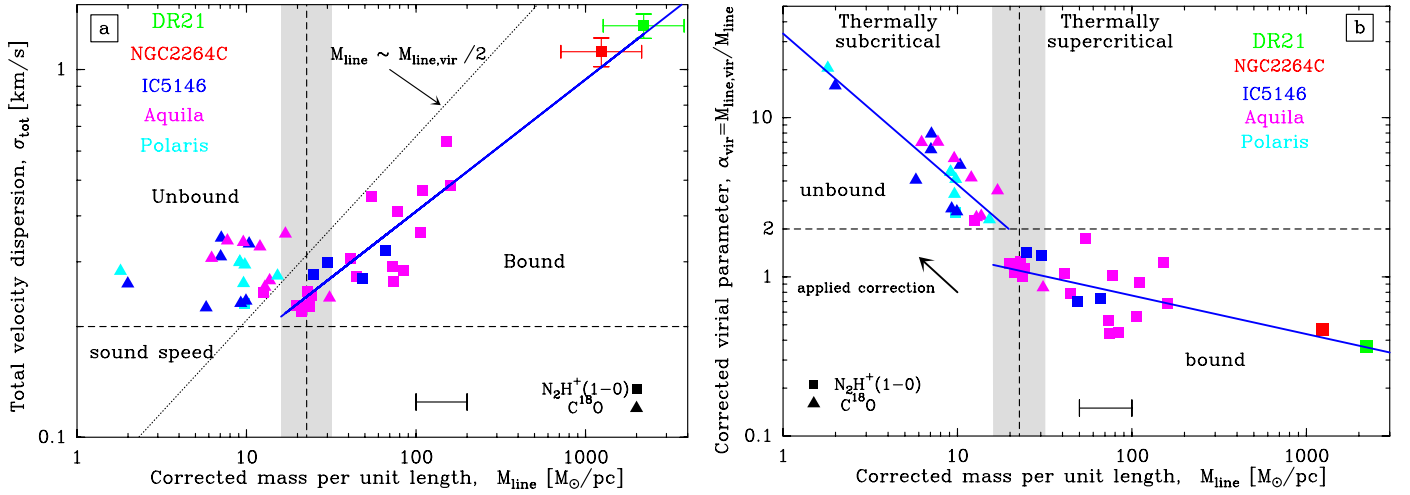


Fig. 7. **a)** Total velocity dispersion versus intrinsic mass per unit length (corrected for inclination effects) for the sample of 46 filaments. The symbols and colors, as well as the y -axis of the plot, are the same as in Fig. 6. The horizontal segment at the bottom of the plot shows the typical error bar on the estimated masses per unit length. Specific error bars are shown for NGC 2264C and DR21 since they are larger⁵. The horizontal dashed line shows the value of the thermal sound speed $\sim 0.2 \text{ km s}^{-1}$ for $T_{\text{gas}} = 10 \text{ K}$. The vertical grey band marks the theoretical position of the effective critical mass per unit length $M_{\text{line,crit}}^{\text{eff}}$ for effective temperatures in the range $10 \lesssim T_{\text{eff}} \lesssim 20 \text{ K}$ (see text). The dotted line running from bottom left to top right corresponds to $M_{\text{line}} = M_{\text{line,vir}}/2$, which marks the boundary between unbound and bound filaments located on the left and right hand side of the border line, respectively. The blue solid line, $\sigma_{\text{tot}} \propto M_{\text{line}}^{0.36 \pm 0.07}$, shows the best power-law fit for the bound filaments. The best-fit exponent remains almost unchanged (0.31 ± 0.08) when the fitting is performed after removing DR21 and NGC 2264C from the sample. **b)** Corrected virial parameter ($\alpha_{\text{line,vir}}$) versus intrinsic mass per unit length for the same filaments (x -axis is the same as in panel **a**). The vertical grey band is the same as in panel **a**) and separates subcritical filaments ($M_{\text{line}}^{\text{obs}} < M_{\text{line,crit}}^{\text{eff}}$) on the left from supercritical filaments ($M_{\text{line}}^{\text{obs}} > M_{\text{line,crit}}^{\text{eff}}$) on the right. The horizontal dashed line ($\alpha_{\text{line,vir}} = 2$) shows the boundary between gravitationally unbound ($\alpha_{\text{line,vir}} > 2$) and bound ($\alpha_{\text{line,vir}} < 2$) filaments, where $\alpha_{\text{line,vir}} = M_{\text{line,vir}}/M_{\text{line}}^{\text{obs}}$. The two blue solid lines show the best fits for the subcritical and supercritical filaments, respectively (see text for details).

intrinsic mass per unit length obtained from the observed value after applying a 60% correction factor to account for the average overestimation of the intrinsic column density due to projection effects. This panel can be divided into two parts by comparing the intrinsic mass per unit length to the virial mass per unit length $M_{\text{line,vir}} = 2\sigma_{\text{tot}}^2/G$ (Fiege & Pudritz 2000), where σ_{tot} is the observed total velocity dispersion (instead of the thermal sound speed used in the expression of $M_{\text{line,crit}}$). The dividing line is defined by $M_{\text{line,vir}} = 2M_{\text{line}}^{\text{obs}}$ equivalent to $\alpha_{\text{line,vir}} = 2$, where

$$\alpha_{\text{line,vir}} = M_{\text{line,vir}}/M_{\text{line}}^{\text{obs}} \quad (6)$$

is the virial parameter of a filament⁷.

Figure 7b shows how the virial parameter depends on the intrinsic mass per unit length for our sample of filaments. This plot (Fig. 7b) can be divided into four quadrants. The effective critical mass per unit length $M_{\text{line,crit}}^{\text{eff}} = 2\sigma_{\text{tot}}^{\text{eff}2}/G$ divides the sample into subcritical filaments on the left-hand side and supercritical filaments on the right-hand side⁸. Conceptually, we define $\sigma_{\text{tot}}^{\text{eff}}$ as the total velocity dispersion of a filament on the verge of global radial collapse. Observationally, the range of internal velocity dispersions σ_{tot} measured here for thermally subcritical and nearly critical filaments suggests that $\sigma_{\text{tot}}^{\text{eff}}$ corresponds to effective temperatures $T_{\text{eff}} \equiv \mu m_{\text{H}} \sigma_{\text{tot}}^{\text{eff}2}/k_{\text{B}}$ in the

⁷ For a sphere of uniform density $\alpha_{\text{vir}} = M_{\text{vir}}/M$ where $M_{\text{vir}} \sim 5R\sigma^2/G$ and M is the mass of the object (e.g., Bertoldi & McKee 1992).

⁸ In this paper, we use the terms “supercritical” and “subcritical” to characterize the mass per unit length of a filament, independently of the magnetic field strength (but see Fiege & Pudritz 2000 for how $M_{\text{line,crit}}$ is modified in the presence of magnetic fields). This should not be confused with the terms “(magnetically) supercritical and subcritical” used to characterize clouds with supercritical and subcritical mass-to-flux ratios, respectively.

range $10 \lesssim T_{\text{eff}} \lesssim 20 \text{ K}$. This implies an effective critical mass per unit length $M_{\text{line,crit}}^{\text{eff}}$ in the range between ~ 16 and $32 M_{\odot}/\text{pc}$, which is shown as a grey band in the plots of Figs. 7a and b. The virial parameter, $\alpha_{\text{line,vir}}$, divides the sample of filaments into unbound ($\alpha_{\text{line,vir}} > 2$) structures in the upper part of the diagram and gravitationally bound structures ($\alpha_{\text{line,vir}} < 2$) in the lower part of the diagram. The virial parameter decreases as $\alpha_{\text{line,vir}} \propto M_{\text{line}}^{-0.95 \pm 0.12}$ for the subcritical filaments, while this dependence is much shallower, $\alpha_{\text{line,vir}} \propto M_{\text{line}}^{-0.24 \pm 0.29}$, for the supercritical filaments of our sample. The best-fit power law exponent for the supercritical filaments remains almost unchanged (-0.28 ± 0.30) when the linear fitting is performed after removing DR21 and NGC 2264C from the sample. Figure 7b indicates that thermally supercritical filaments tend to be gravitationally bound with $\alpha_{\text{line,vir}} = 1.0 \pm 0.5$ on average, and that, conversely, all thermally subcritical filaments are unbound with $\alpha_{\text{line,vir}} > 2$.

6. Discussion and conclusions

The results of our ^{13}CO , C^{18}O , and N_2H^+ line observations toward a sample of filaments previously detected with *Herschel* show that, to an excellent approximation, interstellar filaments may be divided into bound and unbound structures depending on whether their mass per unit length M_{line} is larger or smaller than the thermal value of the critical mass per unit length $M_{\text{line,crit}} = 2c_s^2/G$. Indeed, thermally supercritical filaments are found to be self-gravitating structures in rough virial balance with $M_{\text{line}}^{\text{obs}} \sim M_{\text{line,vir}}$, while thermally subcritical filaments appear to be unbound structures with $M_{\text{line}}^{\text{obs}} \leq M_{\text{line,vir}}/2$ and transonic line-of-sight velocity dispersions ($c_s \lesssim \sigma_{\text{tot}} < 2c_s$). This confirms the usefulness of the simple gravitational instability criterion based on $M_{\text{line,crit}}$ which was adopted by André et al. (2010) in their analysis of the first results from the HGBS.

The detection, in the same cloud (e.g. Aquila), of both subcritical and supercritical filaments, with transonic and supersonic velocity dispersions respectively, suggests that the internal velocity dispersion within a filament is not directly related to the level of large-scale turbulence in the parent cloud. Instead, we propose that the internal velocity dispersion partly reflects the evolutionary state of a filament (see below).

6.1. An evolutionary scenario for interstellar filaments?

In the light of the results presented in this paper, we may revisit the issue of the formation and evolution of interstellar filaments and improve the scenario proposed in our earlier work based on HGBS observations (e.g. Arzoumanian et al. 2011).

The observed omnipresence of filamentary structures in gravitationally unbound complexes such as the Polaris translucent cloud (Men'shchikov et al. 2010; Miville-Deschênes et al. 2010; Ward-Thompson et al. 2010) suggests that large-scale turbulence rather than large-scale gravity play the dominant role in forming interstellar filaments. The finding of a characteristic filament width ~ 0.1 pc (Arzoumanian et al. 2011), corresponding to better than a factor of ~ 2 to the sonic scale below which interstellar turbulence becomes subsonic in diffuse molecular gas (cf. Goodman et al. 1998; Falgarone et al. 2009; Federrath et al. 2010), also supports the view that filaments may form by turbulent compression of interstellar gas (Padoan et al. 2001). In such a picture, filaments coincide with stagnation gas associated with regions of locally converging turbulent motions, where compression is at a maximum and relative velocity differences at a minimum, and are thus expected to have relatively low (transonic) internal velocity dispersions (cf. Klessen et al. 2005). The line-of-sight velocity dispersions measured here for subcritical filaments, which all are in the range $c_s \lesssim \sigma_{\text{tot}} \lesssim 2c_s$, are consistent with this picture. Moreover, our $^{13}\text{CO}(2-1)$ and $\text{C}^{18}\text{O}(2-1)$ mapping results for filament 14 in IC 5146 (cf. Figs. 3 and 5 – see also Hacar & Tafalla 2011 for other filaments in Taurus) suggest that subcritical filaments are velocity-coherent structures in MCs, with small and roughly constant velocity dispersion along their length (cf. Goodman et al. 1998; Heyer et al. 2009, for the definition of the concept of coherence in the context of dense cores).

Since subcritical filaments are unbound, they may be expected to widen and disperse on a turbulent crossing time. Given the mean velocity dispersion $\overline{\sigma}_{\text{tot}} \sim 0.3 \text{ km s}^{-1}$ measured here for subcritical filaments, the typical crossing time of a ~ 0.1 -pc-wide filament is ~ 0.3 Myr. Subcritical filaments may be expected to disperse on this timescale unless they are confined by some external pressure as suggested by Fischera & Martin (2012). These authors modeled interstellar filaments as quasi-equilibrium isothermal structures in pressure balance with a typical ambient ISM pressure $P_{\text{ext}} \sim 2-5 \times 10^4 \text{ K cm}^{-3}$ (Fischera & Martin 2012). The predicted widths of their model filaments are in rough agreement with the observed filament width of ~ 0.1 pc. Moreover, the agreement between the expected and the observed widths improves when polytropic models of pressure-confined filaments, obeying a non-isothermal equation of state $P \propto \rho^\gamma$ with $\gamma < 1$ are considered (Inutsuka, priv. comm.).

The observed increase in velocity dispersion with increasing central column density for thermally supercritical filaments, roughly consistent with the scaling $\sigma_{\text{tot}} \propto N_{\text{H}_2}^{0.5}$ (cf. Fig. 6), provides interesting clues to the evolution of dense, star-forming filaments. Since the filaments on the right-hand side of Fig. 6 have $\alpha_{\text{line, vir}} \sim 1$ and are self-gravitating (see Sect. 5), they should be unstable to radial collapse and thus have a natural tendency

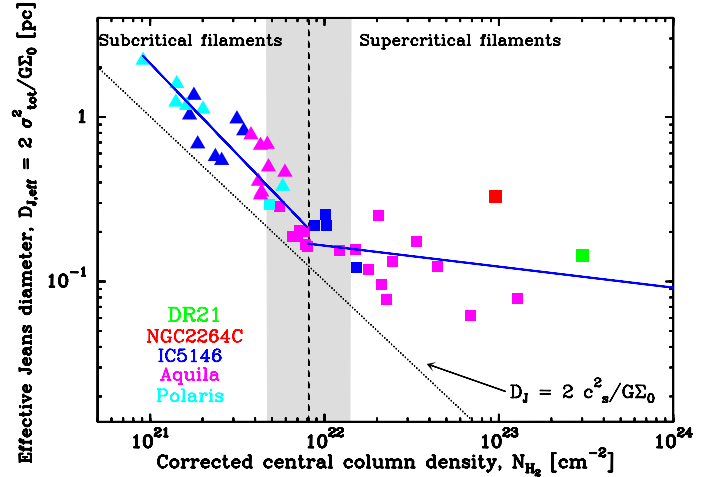


Fig. 8. Effective Jeans diameter ($D_{J,\text{eff}} = 2\sigma_{\text{tot}}^2/G\Sigma_0$) versus filament intrinsic central column density. The vertical dashed line and the grey band mark the border zone between subcritical and supercritical filaments (cf. Fig. 6). The dotted line running from the top left to the bottom right corresponds to the thermal Jeans diameter ($2R_J$). The blue solid lines correspond to the best fits for the subcritical ($D_{J,\text{eff}}^{\text{sub}} \propto N_{\text{H}_2}^{-1.1 \pm 0.1}$) and supercritical ($D_{J,\text{eff}}^{\text{sup}} \propto N_{\text{H}_2}^{-0.2 \pm 0.1}$) filament subsamples, respectively. The exponent of the power-law fit for the supercritical filaments becomes -0.4 ± 0.1 after excluding DR21 and NGC2264C from the sample. In contrast to the thermal Jeans length, the effective Jeans diameter of the supercritical filaments remains roughly constant with an average value of 0.14 ± 0.07 pc.

to contract with time (cf. Inutsuka & Miyama 1992; Kawachi & Hanawa 1998). The shape of their radial column density profiles with a high degree of symmetry about the filament major axis and a well-defined power law regime at large radii, approximately consistent with a radial density structure $\rho \propto r^{-2}$ (Arzoumanian et al. 2011; Palmeirim et al. 2013; Hill et al. 2012), is consistent with a theoretical model of a nearly isothermal collapsing cylinder (Kawachi & Hanawa 1998; Palmeirim et al. 2013), and therefore also suggestive of gravitational contraction. If supercritical filaments are indeed contracting, then their central column density is expected to increase with time (cf. Kawachi & Hanawa 1998). It is thus tempting to suggest that the right-hand side of Fig. 6 may, at least partly, represent an evolutionary sequence for supercritical filaments, in which central column density corresponds to an evolutionary indicator, increasing with time. As the internal velocity dispersion of a filament provides a direct measure of its virial mass per unit length and supercritical filaments have $M_{\text{line}} \gtrsim M_{\text{line, vir}}$, the trend seen on the right-hand side of Fig. 6 suggests that the mass per unit length of supercritical filaments increases with time through accretion of background material. More direct evidence of this accretion process and growth in mass per unit length for supercritical filaments exists in several cases in the form of low-density striations or subfilaments observed perpendicular to the main filaments and apparently feeding them from the side. Examples include the B211/B213 filament in Taurus where the typical velocities expected for the infalling material are consistent with the existing kinematical constraints from CO observations (Goldsmith et al. 2008; Palmeirim et al. 2013), the Musca filament (Cox et al. 2013, in prep.), and the DR21 ridge in Cygnus X (Schneider et al. 2010).

If such an accretion process accompanied by an increase in internal velocity dispersion does indeed occur in supercritical filaments, it may explain how these filaments can maintain a roughly constant inner width while contracting. In collapse

models of nearly-isothermal cylindrical filaments (cf. [Inutsuka & Miyama 1992](#); [Kawachi & Hanawa 1998](#)), the flat inner portion of the radial density profile has a radius corresponding to the instantaneous central Jeans length $R_J \sim c_s^2/G\Sigma_0$, where Σ_0 is again the central mass column density of the model filament. In the presence of a nonthermal component to the velocity dispersion, we may thus expect the central diameter of a contracting filament to be roughly given by twice the effective Jeans length, i.e., $2R_{J,\text{eff}} \equiv D_{J,\text{eff}} \sim 2\sigma_{\text{tot}}^2/G\Sigma_0$. This effective Jeans diameter is plotted in [Fig. 8](#) as a function of corrected central column density for the sample of filaments studied in the present paper. It can be seen in [Fig. 8](#) that $D_{J,\text{eff}}$ is approximately constant for the thermally supercritical filaments in our sample, with an average value of 0.14 ± 0.07 pc.

In this scenario, the enhanced velocity dispersions measured for thermally supercritical filaments would not directly arise from large-scale interstellar turbulence but from the accretion of ambient cloud gas and the gravitational amplification of initial velocity fluctuations through the conversion of gravitational energy into kinetic energy during the accretion and contraction process (see, e.g., the numerical simulations presented by [Peretto et al. 2007](#), to explain the observed characteristics of NGC 2264C). This would also be consistent with the concept of accretion-driven turbulence proposed by [Klessen & Hennebelle \(2010\)](#) to explain the origin of turbulent motions in a wide range of astrophysical objects.

At the same time as they contract and accrete material from the background cloud, supercritical filaments are expected to fragment into cores and form (proto)stars ([Inutsuka & Miyama 1997](#); [Pon et al. 2011](#)). Indeed, for filamentary clouds, fragmentation into cores and subsequent local core collapse occur faster than global cloud collapse ([Kawachi & Hanawa 1998](#); [Pon et al. 2011](#); [Toalá et al. 2012](#)). As pointed out by [Larson \(2005\)](#), the filamentary geometry is thus especially favorable for fragmentation and core formation. This is also supported by observations of supercritical filaments which are usually found to harbor several prestellar cores and Class 0/Class I protostars along their length (cf. [André et al. 2010](#)). Core formation is particularly well documented in the case of the B211/B213 filament in Taurus ([Schmalzl et al. 2010](#); [Onishi et al. 2002](#)) or the Serpens South filament in the Aquila Rift ([Gutermuth et al. 2008](#); [Maury et al. 2011](#)).

To assess the reliability of this tentative scenario for filament formation and evolution, comparison with dedicated numerical simulations would be very valuable. More extensive molecular line mapping of a larger sample of filaments are also very desirable, in order to set stronger observational constraints on the dynamics of these structures.

Acknowledgements. D.A. wishes to thank the staff at the IRAM 30 m telescope at Pico Veleta for the support during the observations and Q. Nguyễn Lưỡng for his help in reducing the IRAM 30 m data using GILDAS/CLASS. This work has benefited from the support of the European Research Council under the European Union's Seventh Framework Programme (Grant Agreement No. 291294) and of the French National Research Agency (Grant No. ANR-11-BS56-0010).

References

André, P., Men'shchikov, A., Bontemps, S., et al. 2010, *A&A*, 518, L102
 André, P., Men'shchikov, A., Könyves, V., & Arzoumanian, D. 2011, in *Computational Star Formation*, eds. J. Alves, B. G. Elmegreen, J. M. Girart, & V. Trimble, IAU Symp., 270, 255

Arzoumanian, D., André, P., Didelon, P., et al. 2011, *A&A*, 529, L6
 Bertoldi, F., & McKee, C. F. 1992, *ApJ*, 395, 140
 Bontemps, S., André, P., Könyves, V., et al. 2010, *A&A*, 518, L85
 Bourke, T. L., Myers, P. C., Caselli, P., et al. 2012, *ApJ*, 745, 117
 Carter, M., Lazareff, B., Maier, D., et al. 2012, *A&A*, 538, A89
 Falgarone, E., Pety, J., & Hily-Blant, P. 2009, *A&A*, 507, 355
 Federrath, C., Roman-Duval, J., Klessen, R. S., Schmidt, W., & Mac Low, M. 2010, *A&A*, 512, A81
 Fiege, J. D., & Pudritz, R. E. 2000, *MNRAS*, 311, 85
 Fischera, J., & Martin, P. G. 2012, *A&A*, 542, A77
 Galli, D., Walmsley, M., & Gonçalves, J. 2002, *A&A*, 394, 275
 Goldsmith, P. F., Heyer, M., Narayanan, G., et al. 2008, *ApJ*, 680, 428
 Goodman, A. A., Barranco, J. A., Wilner, D. J., & Heyer, M. H. 1998, *ApJ*, 504, 223
 Griffin, M. J., Abergel, A., Abreu, A., et al. 2010, *A&A*, 518, L3
 Gutermuth, R. A., Bourke, T. L., Allen, L. E., et al. 2008, *ApJ*, 673, L151
 Hacar, A., & Tafalla, M. 2011, *A&A*, 533, A34
 Heiderman, A., Evans, II, N. J., Allen, L. E., Huard, T., & Heyer, M. 2010, *ApJ*, 723, 1019
 Hennebelle, P., Banerjee, R., Vázquez-Semadeni, E., Klessen, R. S., & Audit, E. 2008, *A&A*, 486, L43
 Hennemann, M., Motte, F., Schneider, N., et al. 2012, *A&A*, 543, L3
 Henning, T., Linz, H., Krause, O., et al. 2010, *A&A*, 518, L95
 Heyer, M., Krawczyk, C., Duval, J., & Jackson, J. M. 2009, *ApJ*, 699, 1092
 Hill, T., Motte, F., Didelon, P., et al. 2011, *A&A*, 533, A94
 Hill, T., André, P., Arzoumanian, D., et al. 2012, *A&A*, 548, L6
 Hily-Blant, P. 2004, Ph.D. Thesis
 Hily-Blant, P., & Falgarone, E. 2009, *A&A*, 500, L29
 Inutsuka, S.-I., & Miyama, S. M. 1992, *ApJ*, 388, 392
 Inutsuka, S., & Miyama, S. M. 1997, *ApJ*, 480, 681
 Johnstone, D., Di Francesco, J., & Kirk, H. 2004, *ApJ*, 611, L45
 Kawachi, T., & Hanawa, T. 1998, *PASJ*, 50, 577
 Klessen, R. S., & Hennebelle, P. 2010, *A&A*, 520, A17
 Klessen, R. S., Ballesteros-Paredes, J., Vázquez-Semadeni, E., & Durán-Rojas, C. 2005, *ApJ*, 620, 786
 Könyves, V., André, P., Men'shchikov, A., et al. 2010, *A&A*, 518, L106
 Lada, C. J., Lombardi, M., & Alves, J. F. 2010, *ApJ*, 724, 687
 Larson, R. B. 2005, *MNRAS*, 359, 211
 Li, D., & Goldsmith, P. F. 2012, *ApJ*, 756, 12
 Mac Low, M., & Klessen, R. S. 2004, *Rev. Mod. Phys.*, 76, 125
 Maury, A. J., André, P., Men'shchikov, A., Könyves, V., & Bontemps, S. 2011, *A&A*, 535, A77
 Men'shchikov, A., André, P., Didelon, P., et al. 2010, *A&A*, 518, L103
 Miettinen, O. 2012, *A&A*, 540, A104
 Miville-Deschênes, M., Martin, P. G., Abergel, A., et al. 2010, *A&A*, 518, L104
 Molinari, S., Swinyard, B., Bally, J., et al. 2010, *A&A*, 518, L100
 Motte, F., Bontemps, S., Schilke, P., et al. 2007, *A&A*, 476, 1243
 Motte, F., Zavagno, A., Bontemps, S., et al. 2010, *A&A*, 518, L77
 Myers, P. C. 1983, *ApJ*, 270, 105
 Myers, P. C. 2009, *ApJ*, 700, 1609
 Onishi, T., Mizuno, A., Kawamura, A., Tachihara, K., & Fukui, Y. 2002, *ApJ*, 575, 950
 Ostriker, J. 1964, *ApJ*, 140, 1056
 Padoan, P., Juvela, M., Goodman, A. A., & Nordlund, Å. 2001, *ApJ*, 553, 227
 Palmeirim, P., André, P., Kirk, J., et al. 2013, *A&A*, 550, A38
 Peretto, N., André, P., & Belloche, A. 2006, *A&A*, 445, 979
 Peretto, N., Hennebelle, P., & André, P. 2007, *A&A*, 464, 983
 Peretto, N., André, P., Könyves, V., et al. 2012, *A&A*, 541, A63
 Pilbratt, G. L., Riedinger, J. R., Passvogel, T., et al. 2010, *A&A*, 518, L1
 Pineda, J. E., Goodman, A. A., Arce, H. G., et al. 2011, *ApJ*, 739, L2
 Poglitsch, A., Waelkens, C., Geis, N., et al. 2010, *A&A*, 518, L2
 Pon, A., Johnstone, D., & Heitsch, F. 2011, *ApJ*, 740, 88
 Roy, A., Martin, P. G., Polychroni, D., et al. 2013, *ApJ*, 763, 55
 Schmalzl, M., Kainulainen, J., Quanz, S. P., et al. 2010, *ApJ*, 725, 1327
 Schneider, S., & Elmegreen, B. G. 1979, *ApJS*, 41, 87
 Schneider, N., Csengeri, T., Bontemps, S., et al. 2010, *A&A*, 520, A49
 Schuster, K.-F., Boucher, C., Brunswig, W., et al. 2004, *A&A*, 423, 1171
 Starck, J. L., Donoho, D. L., & Candès, E. J. 2003, *A&A*, 398, 785
 Toalá, J. A., Vázquez-Semadeni, E., & Gómez, G. C. 2012, *ApJ*, 744, 190
 Ward-Thompson, D., Kirk, J. M., André, P., et al. 2010, *A&A*, 518, L92
 Wilson, T. L., & Rood, R. 1994, *ARA&A*, 32, 191
 Wu, Y., Liu, T., Meng, F., et al. 2012, *ApJ*, 756, 76

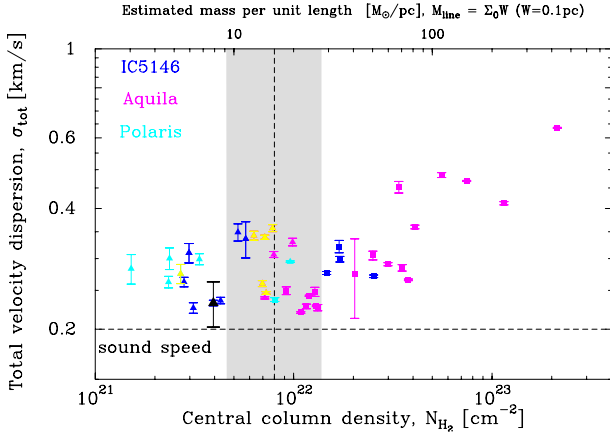


Fig. A.1. Total velocity dispersion versus observed central column density. Similar plot to Fig. 6 for the filaments observed in IC 5146, Aquila and Polaris. The six C^{18}O spectra showing two or three velocity components are flagged in yellow.

Appendix A: Velocity components of the observed filaments

The $\text{N}_2\text{H}^+(1-0)$ and $\text{C}^{18}\text{O}(1-0)/(2-1)$ spectra observed toward the sample of filaments studied in this work are shown in Appendix A. The 23 filaments detected in $\text{N}_2\text{H}^+(1-0)$ in Aquila, IC 5146, and Polaris all show a single velocity component (cf. Figs. A.2, A.4, A.6 and A.9). This is consistent with the view that the filaments are velocity coherent structures

(e.g., Hacar & Tafalla 2011). While most of the filaments detected in C^{18}O show one velocity component, some of them show multiple (two or three) C^{18}O velocity components (such as filaments 20, 22, 23, 25, 26 in Aquila and filament 4 in Polaris – see Figs. A.7, A.8 and A.11). Some of these multiple C^{18}O velocity components may be due to line-of-sight mixing of emissions not necessarily tracing the selected filament, but background and/or foreground structures (especially in the case of the Aquila Rift which is a region close to the Galactic plane).

Assuming that interstellar filaments are velocity-coherent structures, the most likely velocity component associated with each filament was considered (selecting the velocity component with the velocity closest to that of neighboring filaments). Its properties were then used in the discussion of the results presented in this paper (see detailed explanations in the captions of the figures presenting the observed spectra).

In order to investigate how the uncertainty in selecting the relevant velocity component affects our results, the 6 filaments with spectra showing more than one C^{18}O velocity component were flagged in the sample. Figure A.1 shows the total velocity dispersion as a function of central column density for the resulting subsample of 38 filaments, where the velocity dispersions of the filaments inferred from the C^{18}O spectra (which show multiple velocity components) corresponding to filaments 20, 22, 23, 25, 26 in Aquila and 4 in Polaris are flagged in yellow. Our general conclusions on filament properties, such as total velocity dispersion, central column density, and mass per unit length remain unchanged whether or not we take the 6 flagged filaments into account.

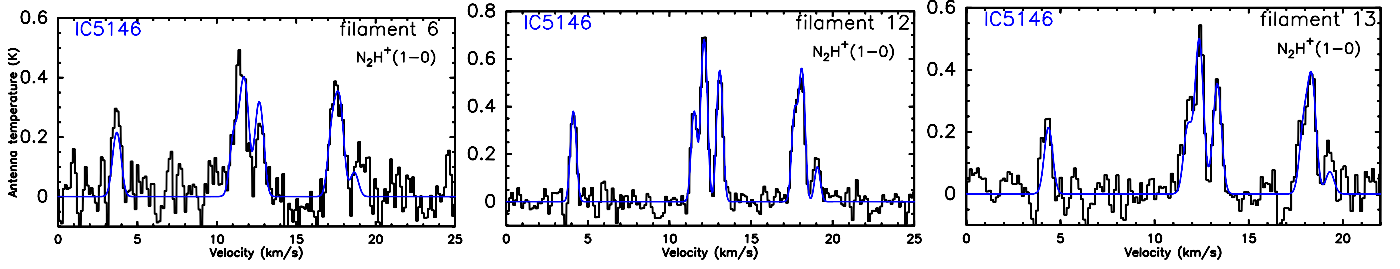


Fig. A.2. $N_2H^+(1-0)$ spectra observed toward filaments 6, 12, 13 in IC 5146. The filament numbers are indicated at the upper right of each panel. The corresponding one velocity hyperfine structure Gaussian fits are highlighted in blue.

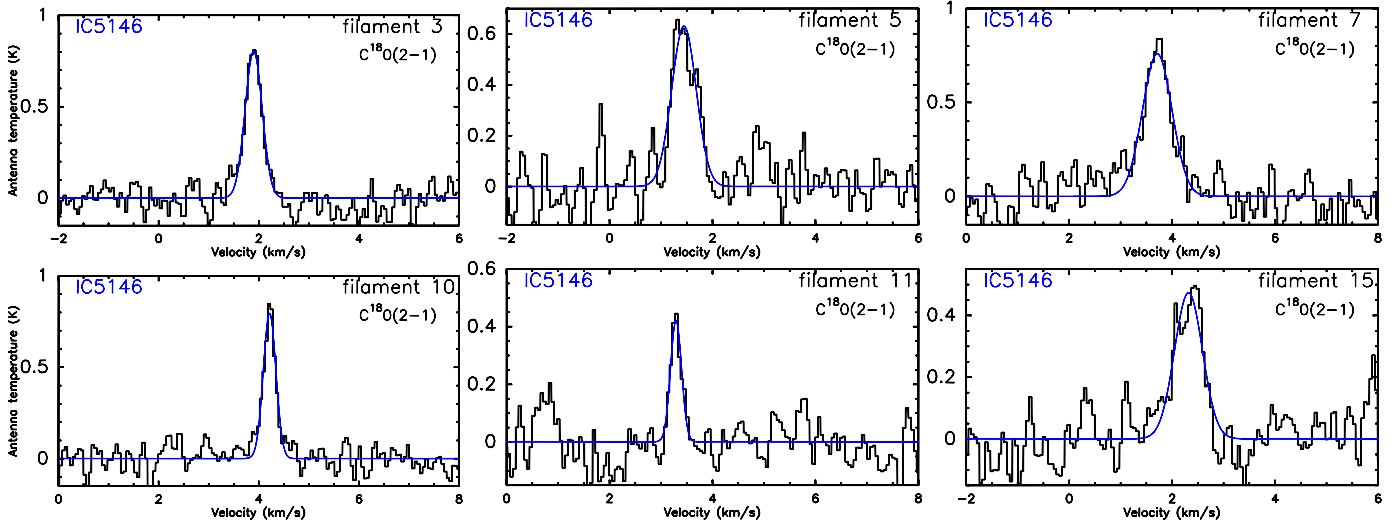


Fig. A.3. $C^{18}O(2-1)$ spectra observed toward 6 filaments in IC 5146. The filament numbers are indicated at the *upper right* of each panel. The corresponding single-component Gaussian fits are highlighted in blue.

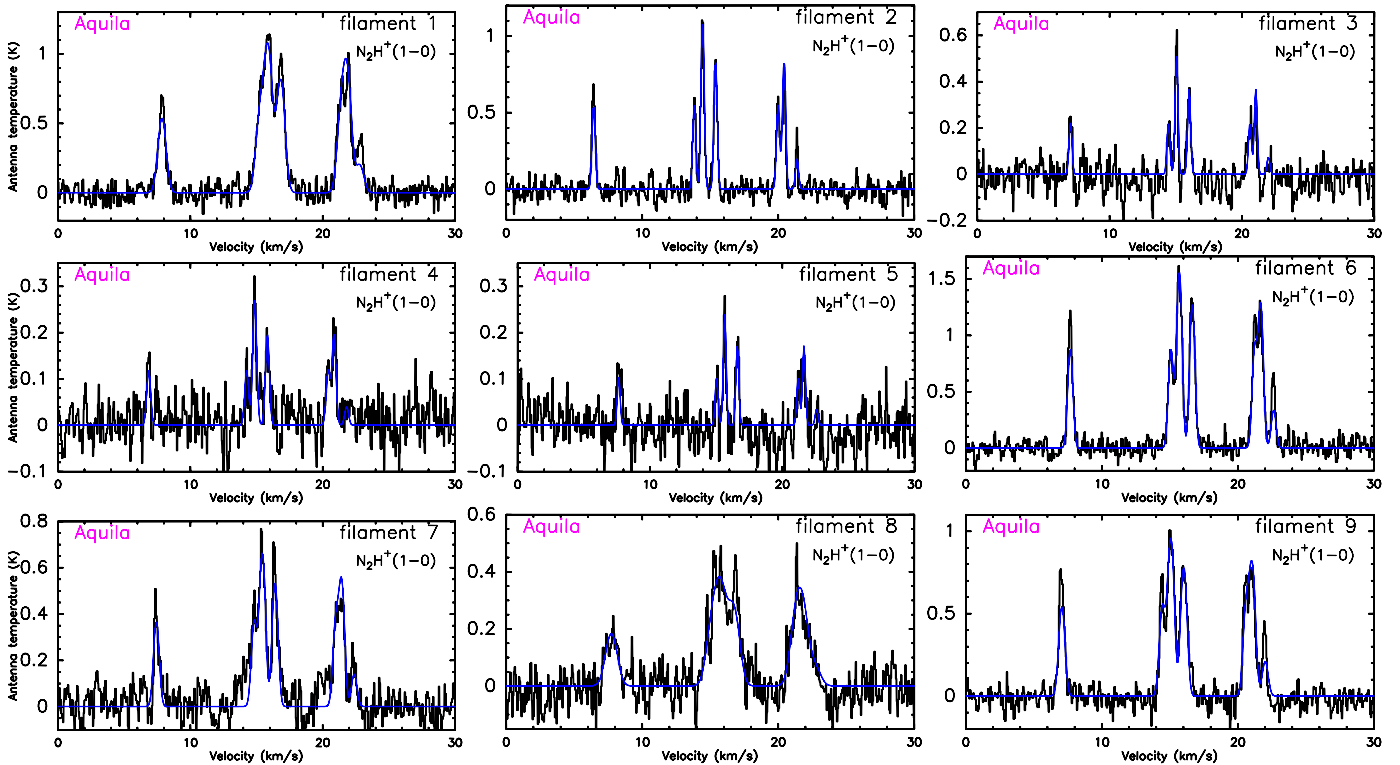


Fig. A.4. $N_2H^+(1-0)$ spectra observed toward 9 filaments in Aquila. The numbers indicated on the upper right hand side of the plots, correspond to the filaments marked on the column density map of Fig. A.5 and listed in Table 1. The corresponding single-component hyperfine structure Gaussian fits are highlighted in blue. Note that the y -axis scale is not the same for all spectra, but has been adjusted to match the peak temperatures which vary between ~ 0.2 to >3 K.

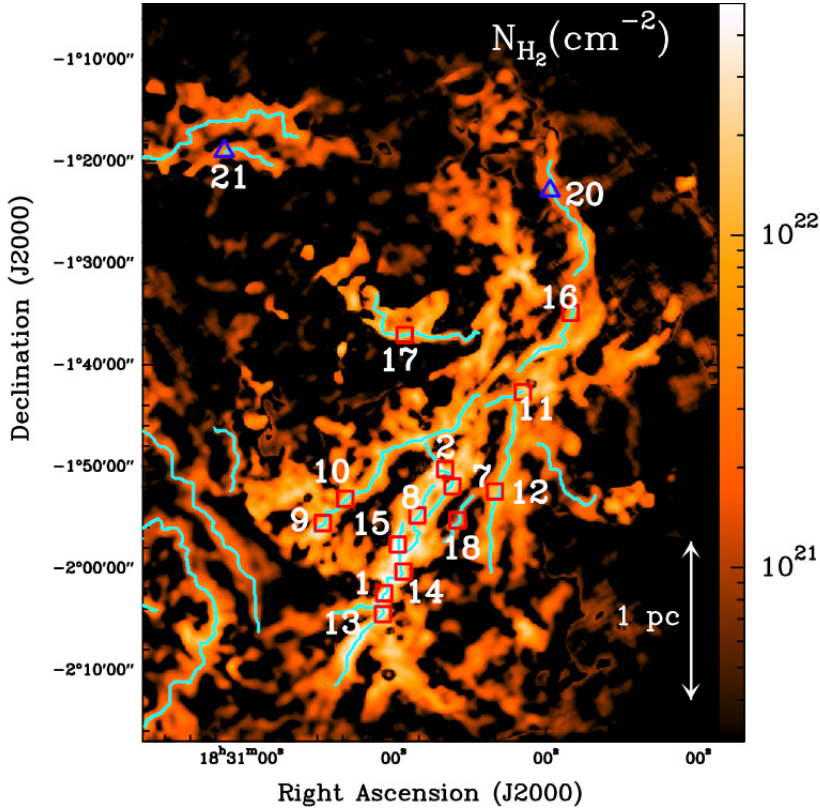


Fig. A.5. Curvelet component of the column density map of the Aquila field around the Serpens South filaments taken from André et al. (2010). The curvelet component is obtained using a morphological component analysis algorithm (MCA, from Starck et al. 2003) which enhances the contrast of the filamentary structure against the more diffuse background of the cloud. The positions of the observed spectra are plotted in red squares and blue triangles for N_2H^+ and C^{18}O , respectively. The numbers correspond to the filaments listed in Table 1 and are given at the upper right of the spectra in Fig. A.4 and some of the spectra of Fig. A.7.

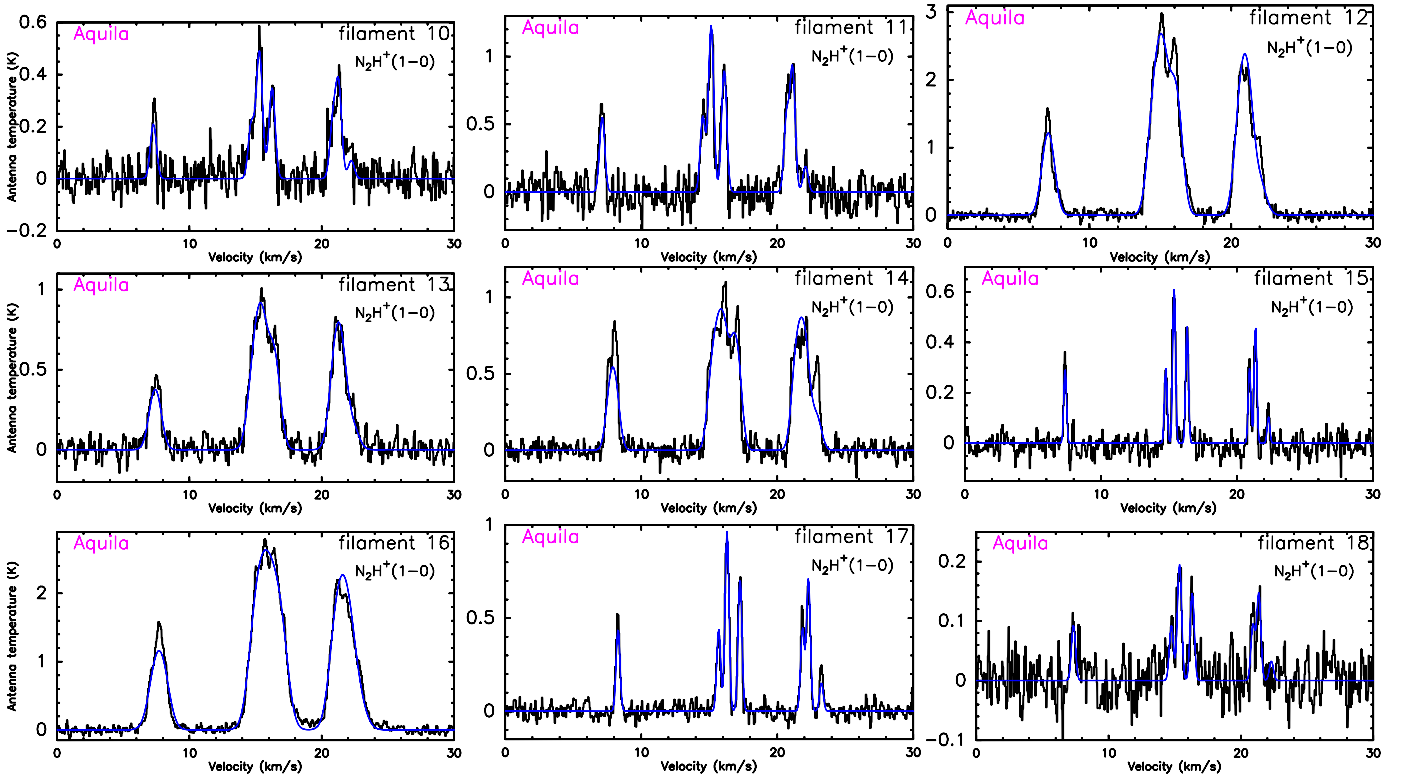


Fig. A.6. Continuation of Fig. A.4 presenting the $\text{N}_2\text{H}^+(1-0)$ spectra observed toward 9 filaments in Aquila.

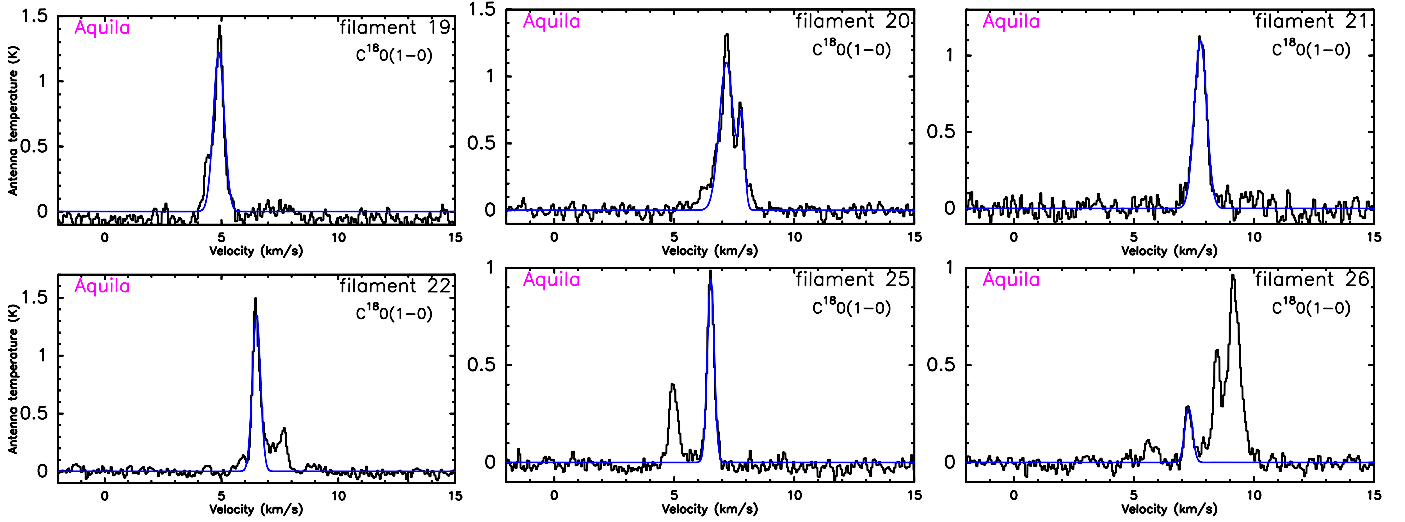


Fig. A.7. $C^{18}O(1-0)$ spectra observed toward 6 filaments in Aquila. The corresponding Gaussian fits are highlighted in blue. Note 1: filament 20 shows two components separated by 0.63 km s^{-1} . The component at $V_{\text{LSR}} = 7.17 \text{ km s}^{-1}$ have been chosen to be tracing the filament, since this component has a velocity component which is closer to the average velocity ($\bar{V}_{\text{LSR}} = 7.4 \text{ km s}^{-1}$) of the filaments in Aquila which show one velocity component. Note 2: the spectrum observed at the position of filament 22 shows two velocity components, one centered at 6.5 km s^{-1} and the other at 7.7 km s^{-1} . The strongest component has been selected for similar reasons to that explained for filament 20. Note 3: the spectrum observed at the position of filament 25 has two velocity components (at 5.0 km s^{-1} and 6.52 km s^{-1} , respectively). The strongest component has been selected for similar reasons to that explained for filament 20. Note 4: the spectrum observed at the position of filament 26 shows three velocity components centered at 7.28 km s^{-1} , 8.45 km s^{-1} and 9.17 km s^{-1} , respectively. The component centered at 7.28 km s^{-1} has been selected because it is the component with the closest V_{LSR} value to the mean \bar{V}_{LSR} of neighboring filaments in Aquila.

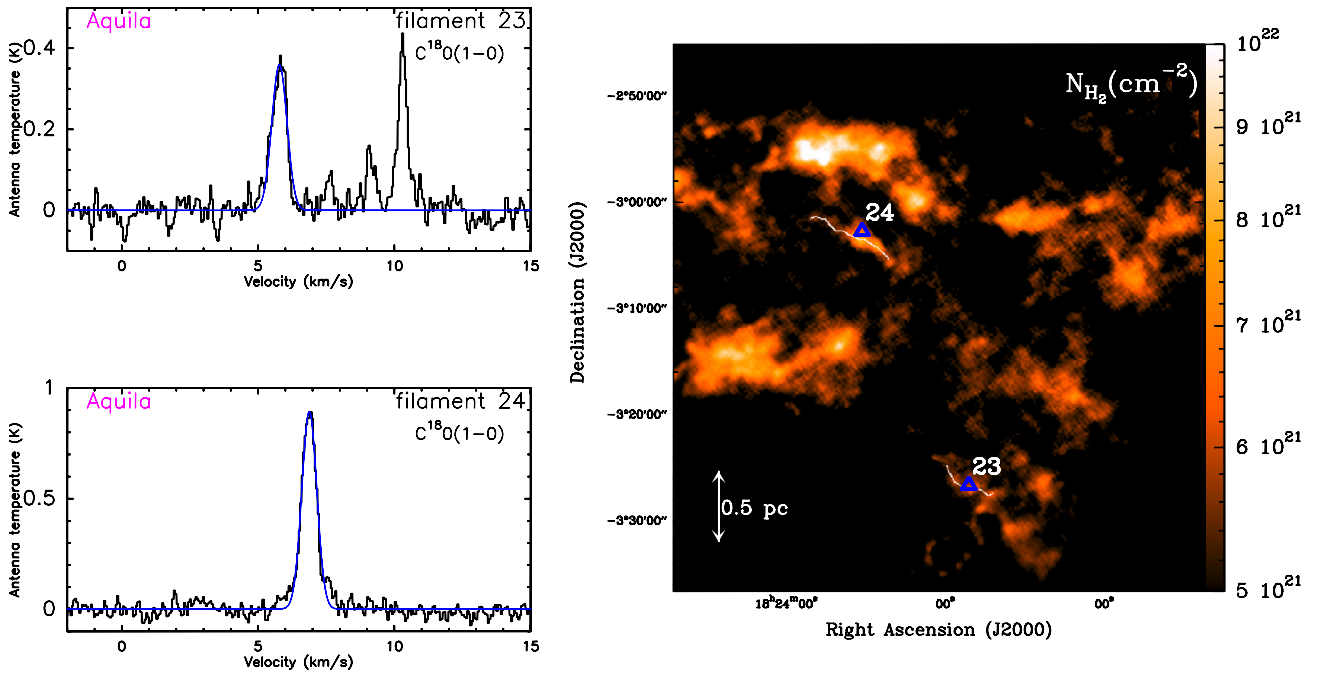


Fig. A.8. $C^{18}O(1-0)$ spectra observed toward filaments 23 and 24 in Aquila, located in the south west part of the region. The positions of the two filaments are shown on a blow up of the column density map (cf., Könyves et al. 2010) on the right hand side. Filament 24 shows a single velocity $C^{18}O(1-0)$ spectrum at $V_{\text{LSR}} = 6.87 \text{ km s}^{-1}$, while $C^{18}O(1-0)$ spectrum observed toward filament 23 shows three velocity components at $V_{\text{LSR}} = 5.77 \text{ km s}^{-1}$, 9.13 km s^{-1} and 10.3 km s^{-1} . The relevant velocity component associated to filament 23 is most probably the component at $V_{\text{LSR}} = 5.77 \text{ km s}^{-1}$ (the closest to the LSR velocity of the neighboring filament 24), while the other components are likely associated to clouds/filaments observed on the same line-of-sight.

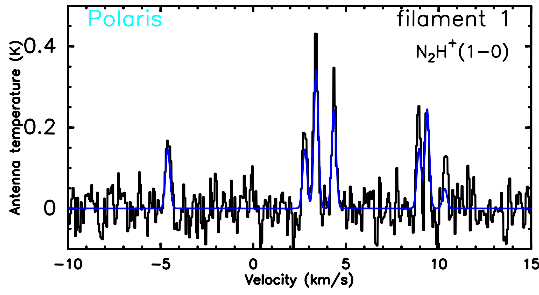


Fig. A.9. $N_2H^+(1-0)$ spectrum observed toward filament 1 in Polaris. The corresponding hyperfine structure Gaussian fit is highlighted in blue.

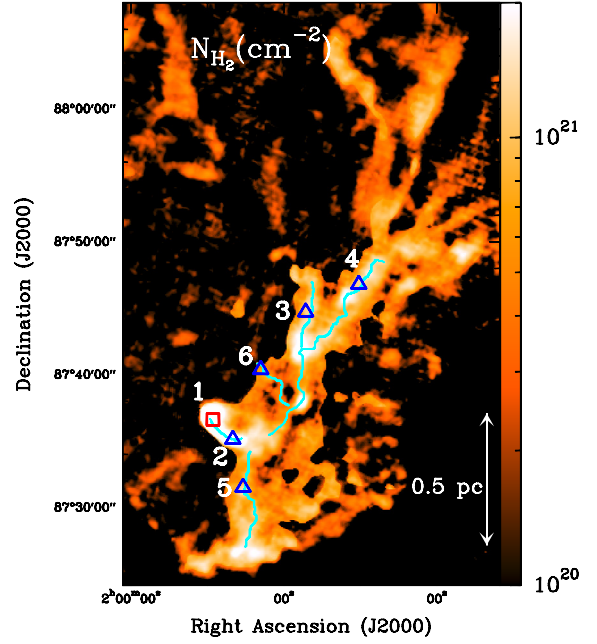


Fig. A.10. Curvlet component of the column density map of a sub-region in the Polaris Cloud taken from André et al. (2010). The positions of the observed spectra are plotted in red squares and blue triangles for N_2H^+ and $C^{18}O$, respectively. The numbers correspond to the filaments listed in Table 1.

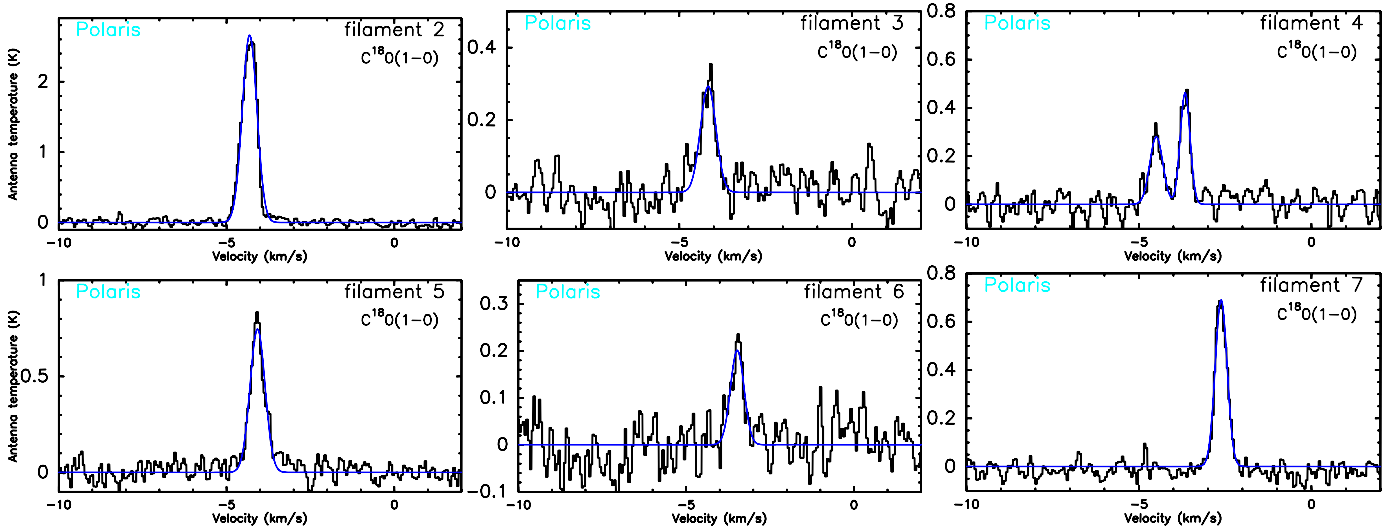


Fig. A.11. $C^{18}O(1-0)$ spectra observed toward 6 filaments in Polaris. The corresponding Gaussian fits are highlighted in blue. Note 1: the spectrum observed toward filament 4 shows two velocity components. Both velocity components have similar linewidths (0.19 km s^{-1} and 0.14 km s^{-1} , respectively), they are separated by $\sim 0.8 \text{ km s}^{-1}$. They most probably belong to two filaments which are seen on the same line-of-sight (but a large map would be needed to study the kinematics of the field). The component observed at -4.5 km s^{-1} has been taken to be representative of filament 4.